



UNIVERSITÄT POTSDAM

MATHEMATISCH NATURWISSENSCHAFTLICHE FAKULTÄT

INSTITUT FÜR PHYSIK UND ASTRONOMIE

The first spectroscopic study of the complete sample of WR stars in the metal poor dwarf galaxy NGC 6822

MASTER THESIS

Submitted in fulfillment of the requirements for the degree of “Master of Science (M.Sc.) Astrophysics” to the department of Physics and Astronomy at the University of Potsdam

submitted to:

APL. PROF. LIDA OSKINOVA

AND

PROF. DR. STEPHAN GEIER

by:

JULIAN STÄHLE

Kaiser Friedrich Str. 147

14469 Potsdam

Student ID: 790548

E-Mail: jstaehle@uni-potsdam.de

May 22, 2023

STATUTORY DECLARATION

I herewith declare that I have composed the present thesis myself and without use of any other than the cited sources and aids. Sentences or parts of sentences quoted literally are marked as such; other references with regard to the statement and scope are indicated by full details of the publications concerned. The thesis in the same or similar form has not been submitted to any examination body and has not been published. This thesis was not yet, even in part, used in another examination or as a course performance.

DECLARATION OF CONSENT

We inform you that, when submitting your master thesis, plagiarism detection software will be used to ensure that your work was written according to the guidelines of scientific work. With your signature you acknowledge this and agree to it.

Potsdam, May 22, 2023

Julian Stähle

Abstract

Context. In the past, Wolf-Rayet (WR) stars have been studied in several local group galaxies. However, there is only a vague understanding of how WR stars behave in metal-poor galaxies. Because of its metal-poor, SMC-like metallicity, NGC 6822, which is also in the local group, is one of the best candidates to test and extend the current research on WR stars and the early universe. The early universe had low metallicity compared to today.

Aim. We analyze and categorize four WR candidates using spectroscopy.

Methods. For this, we use data taken by the Very large Telescope (VLT) in April 2022 and analyse them with the following programs: ESOREFLEX and Potsdam Wolf Rayet Modelling Code (PoWR).

Results. We present a catalog of four WR star spectra and examine [AM85] NGC6822 12 in detail. By doing so, we confirm that this star has no hydrogen and the classification WNE. Furthermore, we discuss the origins of its broad line profile.

Zusammenfassung

Kontext. In der Vergangenheit wurden Wolf Rayet (WR) Sterne in mehreren Galaxien der lokalen Gruppen untersucht. Allerdings, gibt es nur ein vages Verständnis davon, wie sich WR Sterne in metallarmen Galaxien verhalten. Aufgrund ihrer metallarmen, SMC-ähnlichen Metallizität, ist NGC 6822, welche sich ebenfalls in der lokalen Gruppe befindet, einer der besten Kandidaten um die aktuelle Forschung über WR Sterne und das frühe universum zu testen und zu erweitern. Das frühe Universum hatte ebenfalls eine im Vergleich zu heute geringe Metallizität.

Ziel. Wir analysieren und kategorisieren vier WR Stern Kandidaten mithilfe von Spektroskopie.

Methoden. Dafür benutzen wir Daten, die vom Very Large Telescope (VLT) im April 2022 aufgenommen wurden, und analysieren diese mit folgenden Programmen: ESOREFLEX und PoWR.

Ergebnis. Diese Arbeit präsentiert einen spektralen Katalog von vier WR Sternen und die Untersuchung von [AM85] NGC6822 12 im Detail. Dabei bestätigen wir, dass dieser Stern kein Wasserstoff und die Klassifizierung WNE besitzt. Darüber hinaus diskutieren wir die Ursprünge seines besonderen Linienprofils.

Resumen

Contexto. En el pasado, se han estudiado estrellas Wolf-Rayet (WR) en varias galaxias del Grupo Local. Sin embargo, existe solo una comprensión vaga de cómo se comportan las estrellas WR en galaxias pobres en metales. Debido a su baja metalicidad, similar a la de SMC, NGC 6822, que también pertenece al Grupo Local, es uno de los mejores candidatos para poner a prueba y ampliar la investigación actual sobre las estrellas WR y el universo temprano. El universo temprano tenía una baja metalicidad en comparación con la actual.

Objetivo. Analizamos y categorizamos cuatro candidatos a estrellas WR utilizando espectroscopía.

Métodos. Para ello, utilizamos datos obtenidos por el Very large Telescope (VLT) en abril de 2022 y los analizamos con los siguientes programas: ESOREFLEX y Potsdam Wolf Rayet Modelling Code (PoWR).

Resultados. Presentamos un catálogo de cuatro espectros de estrellas WR y examinamos detalladamente a [AM85] NGC6822 12. Al hacerlo, confirmamos que esta estrella no tiene hidrógeno y tiene la clasificación WNE. Además, discutimos los orígenes de su perfil de líneas anchas.

Acknowledgements

Without the following people, my thesis would not be what it is. First of all I want to warmly thank my **parents** who supported me, my whole life and onwards. I can count on them any time which helped me very much especially during the study time.

I really would like to thank Lida Oskinova, Wolf Rainer Hamann, Helge Todt, Stephan Geier, Mauricio, Sabela and Daniel for fruitful discussions, helping me out when I had problems and for having a great time and support in the massive star group at the University of Potsdam. I also want to thank them for the helpful hints they provided to me considering not only the thesis but also scientific work and behavior.

Furthermore, I would like to warmly thank my colleagues and friends who supported me during my physics study time. Among them, special thanks to Ida, Mathurin, Andrew, Coleman, Kyle and Lisa who read over the thesis. I want to thank and mention some people in particular who are important to me and who joined me through this physics journey: Sönke, Alex, Lea, Moritz, Ben, Hans, Nadja, Toni, Ida, Florian R., Lena, Helena, Adonis and the whole Bachelor physics beginners from 2017. Another thank goes to the FSR MaPhy and all my friends outside

physics who supported me, too: Pia B., Kevin, Silco, Pia H., Lara, Sissy, Simon, Skarlett, Anne, Florian K., Paul R. and the HPI Jazz Band. Without all these people I met on my way I would not be where I am now.

Research Acknowledgments This research made use of [hips2fits](#) and [SIMBAD](#), a service provided by CDS.

This research made use of observations collected at the European Southern Observatory under ESO programme 109.2326.001.

This research made use of Hubble Space Telescope images which are cited at the corresponding location. Furthermore, plots were made using Python3 libraries matplotlib (*version 3.3.4*), numpy (*version 1.17.3*), tqdm (*version 4.64.0*), scipy (*version 1.3.3*) and astropy (*version 4.0.2*), Esoreflex and WRplot.

For unknown abbreviations and scientific words or programs, see the Acronyms and Glossary section after the Bibliography. Furthermore, all links to images, manuals etc. can be found after the bibliography section.

Contents

Contents	v
1 Introduction	1
2 Wolf-Rayet Stars	3
2.1 Observed properties and stellar classification	3
2.2 Physical parameters	4
2.3 Attributes of the Wind	7
2.4 Evolutionary models	7
2.5 Current state of research on WR stars	8
3 NGC 6822 - Barnard's Galaxy	11
4 Observations	15
4.1 Methods to detect WR stars	15
4.2 Our observation of the four WR stars	16
4.3 Reduction and extraction with Esoreflex	18
4.4 Photometry	21
5 Spectral analysis and comparison with the model	25
5.1 Spectral library of WR Stars in NGC 6822	25
5.2 In depth analysis of [AM85] NGC6822 12	26
5.3 A few words about the other stars	33
6 Results	37
6.1 [AM85] NGC6822 WR12	37
7 Discussion	41
8 Summary and outlook	43
Acronyms and Glossary	45

Bibliography	47
List of Figures	50
List of Tables	53
Appendix	i

Introduction

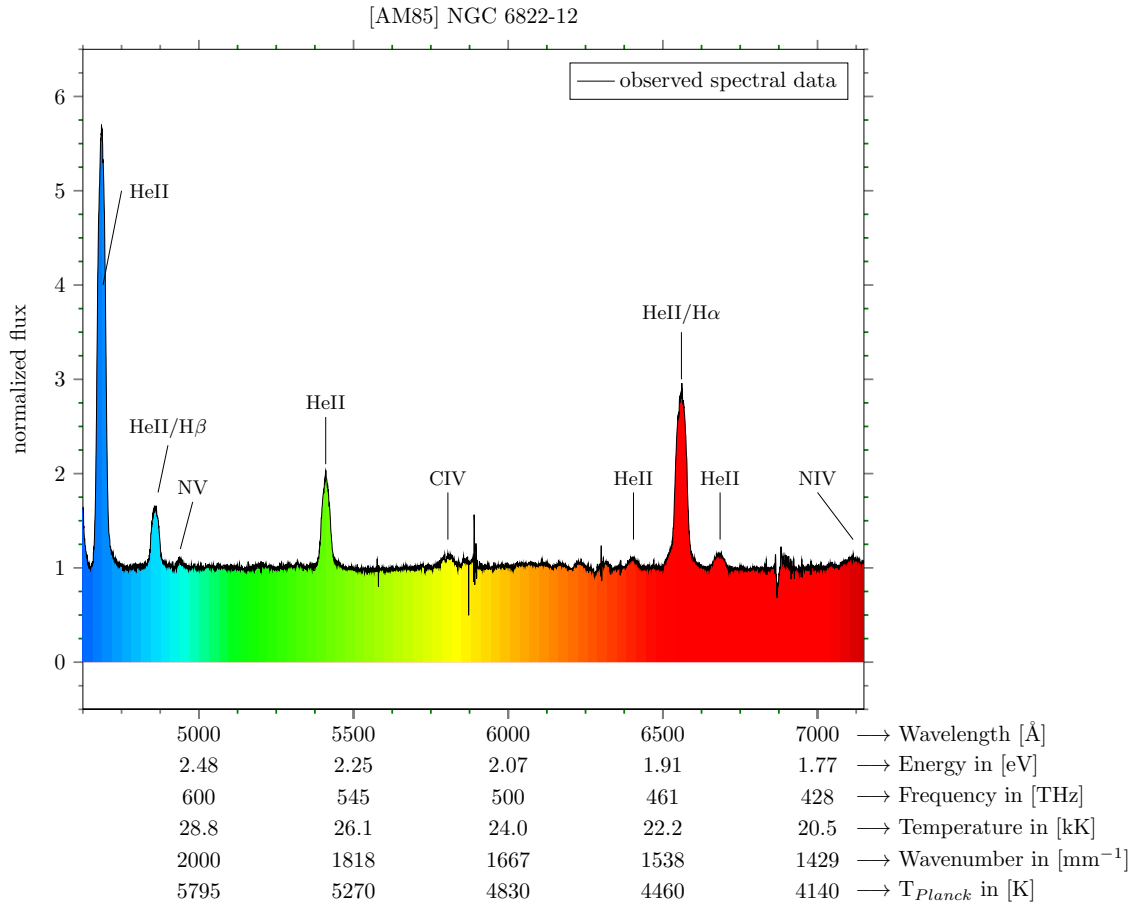
Over 1.3 million years ago, a distant galaxy emitted light that we can observe on Earth today. This light came from Barnard's Galaxy (NGC 6822) which was discovered by Edward Emerson [Barnard \(1884\)](#). NGC 6822 is a member of the local group and is characterized by a particularly low iron content. Other galaxies, such as the Milky Way (MW), the Large Magellanic Cloud (LMC) or the Small Magellanic Cloud (SMC), which are also in the Local Group, have higher iron contents. About 400 million years after the Big Bang, at the time of reionisation, there was less iron present than measured today. Consequently, conclusions about the young universe can be drawn from observations of such galaxies like Barnard's Galaxy. To understand what contributed to the reionisation of hydrogen at that time, we therefore study blue objects, which emit multitudes of radiation into their surroundings.

A special type of object, which contribute to galactic evolution, are Wolf-Rayet (WR) stars. What is special about them is their emission line spectrum. This is produced in stellar winds that are orders of magnitude larger than winds from solar-like stars. These winds supply their surroundings with enriched material and support the chemical evolution of galaxies. Such stars start their life as a massive ($>20 M_{\odot}$) O type and end as a powerful supernovae (SN), forming black holes (BH) or neutron stars (NS). The mechanisms of stellar feedback, (e.g. ionizing radiation, winds and supernovae), induce new star formation in galaxies. WR stars are the bridge between galactic and cosmological scales, as well as drivers of the chemical evolution of galaxies. The study of WR stars is essential if one wants to understand the evolution of the universe, galaxies and also humanity.

This work deals with the classification of four WR stars in the iron-poor irregular galaxy NGC 6822 based on their spectra, which we obtained using observations from ESO's VLT. Furthermore, the spectra of the four stars are modelled with the modelling program: Potsdam Wolf Rayet Modelling Code (PoWR), which is developed in Potsdam. This enables us to characterize all four stars. The spectra are checked for possible binary star systems and compared with the results of previous work. By analyzing WR stars in a metal-poor Galaxy, we try to improve the metallicity (Z) mass loss (\dot{M}) powerlaw relation. This has already been established with data from the LMC, SMC, and the MW ([Sander et al., 2019](#)). In addition, we determine new parame-

ter, put all stars in a Hertzsprung-Russel diagram (HRD) to study ways of possible evolutionary paths of these stars and compare them with stars in the galaxies just mentioned. In chapter 2 we will deal with WR stars and its properties and evolution in general. Furthermore, we will deal with the details of the Barnard's Galaxy in chapter 3. After discussing the theory, we will cover the experimental part. Chapter 4 takes a closer look at the methods of observation, data analysis, and modeling of the observed spectra. Subsequently, the four WR stars are analyzed and evaluated on the basis of their spectra in chapter 5 (see the eye-catching spectrum in Figure 1.1). Chapter 6 summarizes the results of this analysis. Finally, a discussion of the errors, analysis and evaluation methods follows in chapter 7. The master thesis ends with a summary of this research work and gives an outlook on possible future projects in chapter 8.

Figure 1.1: Spectra of [AM85] NGC 6822 12 plotted with the visual colors where dark blue is at 3800 Å and dark red is at 7200 Å. This displays the color range of our eye.



Wolf-Rayet Stars

The WR type of stars were found by two french physicists in 1867. [Wolf & Rayet \(1867\)](#) discovered an at this time, unusual broad Helium emission line spectrum in three stars of the Cygnus constellation. With the discovery of more stars with such phenomenon, it was possible to classify them in more detail and research their evolution. Until now their appearance and behavior is not fully understood and highly debated. [Crowther \(2007\)](#); [Hamann et al. \(2016\)](#); [Shenar \(2022\)](#) give an overview about the current state of the research. This summary is oriented on [Crowther \(2007\)](#). Nowadays, WR stars are researched in the MW ([Sander, A. et al., 2012](#); [van der Hucht, 2001](#)), the SMC ([Hainich et al., 2015](#)) and the LMC ([Hainich, R. et al., 2014](#)).

2.1 Observed properties and stellar classification

Due to these unusual emission lines, there kind of stars are classified after their spectrum and not as other stars, after their temperature and luminosity. The uniqueness comes from broad emission lines while others usually show an absorption spectrum. Nevertheless, WR stars can also contain absorption lines (see [Beals, 1940](#)). A first categorization pattern was introduced by [Smith \(1968\)](#). It was further developed by [van der Hucht \(2001\)](#) where we use it for our analysis of the spectra. The main stellar type in this work are WN-type stars. They contain N III-V lines. The line strength of the nitrogen lines is compared to the He I-II lines in the spectrum. From there, this type can be subdivided into WN-early (WNE or WN2-WN5) and WN-late (WNL or WN7-WN11) types ([van der Hucht, 2001](#)). This can be confusing since from an evolutionary point of view a star which contains hydrogen is earlier in evolution than a star without hydrogen. The details about stellar evolution in general are explained very well in [Kippenhahn et al. \(2014\)](#) for example. There exist also WC and WO types which contain carbon and oxygen lines, respectively. Furthermore, a combination of types (e.g. WN/C) is possible since the classification definitions leave a certain flexibility ([Conti et al., 1989](#)).

2.2 Physical parameters

One possibility to achieve physical parameters from a spectrum and to further characterize a star is to model it. This is what the PoWR program does. PoWR is a modeling program for stellar atmospheres specialized on WR and O stars. It takes into account the radiative transfer equations in a non-local thermal equilibrium (LTE) environment in the co-moving frame as well as line blanketing. [Gräfener et al. \(2002\)](#); [Hamann & Gräfener \(2003\)](#); [Sander et al. \(2015\)](#) contributed and developed this code over decades and still maintain it. Among the assumptions made, it exhibits:

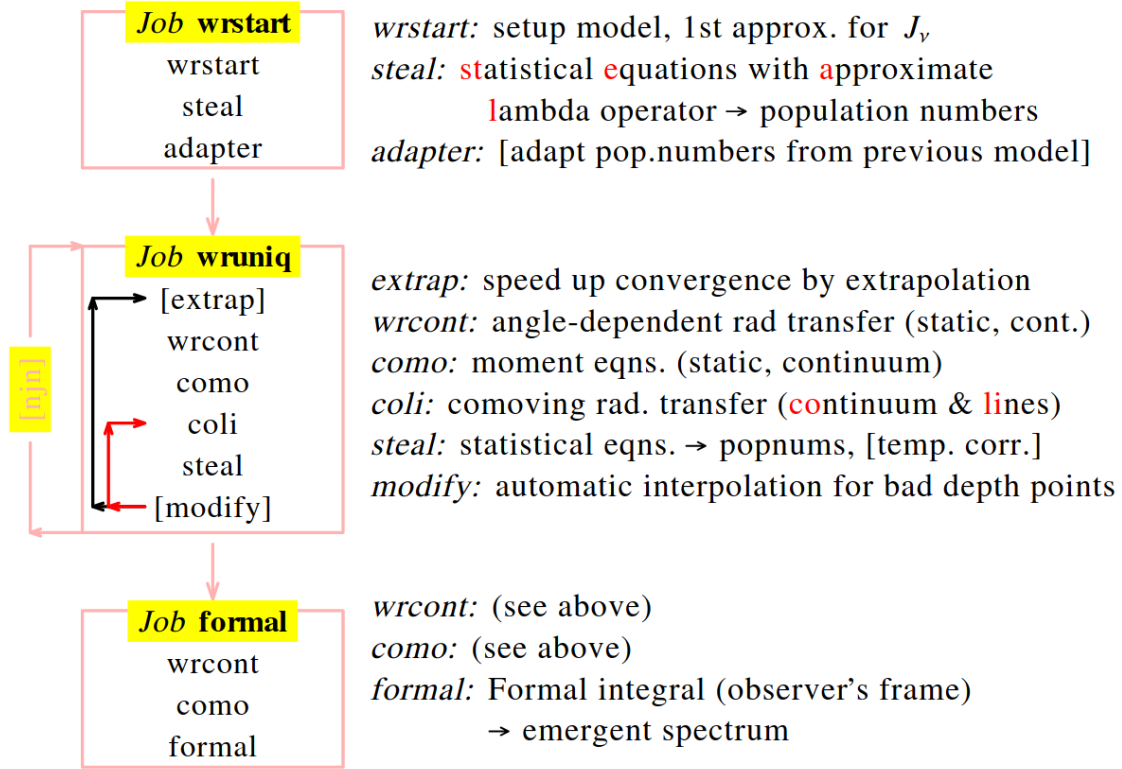
- one dimensional spherically-symmetric expansion,
- stationary and homogeneity,
- clumping in the small scale limit,
- wind velocity including beta law,
- radiative equilibrium which leads to a radius dependent temperature $T(r)$,
- non-LTE radiative transfer

(see [Hamann & Todt, 2023](#)). The workflow of the program can be seen in Figure 2.1. The research group in Potsdam calculated a grid of models for different parameters for different galaxies. This assists scientists to get a first insight of which parameter an observed spectrum has. Since the models have fixed parameters, it is not likely that a grid model fits perfectly to an observation. Thus, one can calculate different models. The time to compute a spectrum with this code takes up to a few days. Therefore, it is useful to know how a spectrum behaves under changing different parameter or under which transformation the spectrum stays the same. With that knowledge, one can make an educated guess and lowers calculation time. In the following, I will introduce the most important parameter and their relations for this work used in the program.

Parameter of the model

The main free parameters which can be changed, are mass loss rate (\dot{M}), luminosity (L), effective temperature (T_*), terminal wind velocity (v_∞) including beta parameters (see equation 2.3), clumping (D) and chemical composition.

Figure 2.1: Structure of a PoWR model calculation from the [PoWR manual](#) (Hamann & Todt, 2023).



Luminosity We assume black body radiation such that Planck's law holds for the luminosity:

$$L_* = 4\pi\sigma R_*^2 T_*^4, \quad (2.1)$$

where R_* is the stellar radius, T_* the photospheric temperature and σ the Stefan-Boltzmann constant. Thus, $L \sim R_*^2$ and $L \sim T_*^4$. The luminosity can be estimated from the Spectral Energy Distribution (SED). This presents the relation between emitted energy (flux) of the star to the wavelength. By aligning the observed spectrum to the photometry of the object the model can be fitted to the observation by eye and thus the luminosity can be obtained. Shapes of the slope are effected by reddening, therefore extinction laws are also applied. We will cover this in detail later in section 4.4.

Rotational velocity of the star The $\nu \sin(i)$ value, (*VSINI*) in PoWR, represents the projected equatorial rotational velocity in km/s. We need to respect the inclination to the star since we cannot know from which side we see the object. The rotational velocity contributes to the formal integral (see Figure 2.1). This job only takes up to a few minutes which is why we can make for several models, multiple rotation guesses and try out which fits the best.

Wind velocity The wind velocity v_∞ can be expressed via

$$v(r) = v_\infty \left(1 - \frac{R_*}{r}\right)^\beta, \quad \text{or} \quad (2.2)$$

$$v(r) = v_\infty \left[q_1 \left(1 - \frac{r_0}{r}\right)^{\beta_1} + q_2 \left(1 - \frac{r_1}{r}\right)^{\beta_2} \right], \quad (2.3)$$

where in the second equation, $q_1 + q_2 = 1$, R_* is the radius of the star and r is either the maximum radius or the connection point radius of wind and photosphere. In equation 2.3, we divide the wind into two parts. Fortunately, the winds we will cover are possible to reconstruct with equation 2.2.

Transformed radius and mass loss rate The transformed radius "... is the ratio between the emission measure of the wind and the area of the stellar surface." (Hamann & Todt, 2023). It can be calculated in the following way:

$$R_t = R_* \left[\frac{v_\infty}{2500 \text{ km s}^{-1}} \cdot \left(\frac{\dot{M} \sqrt{D}}{10^{-4} M_\odot / \text{yr}} \right)^{-1} \right]^{2/3}. \quad (2.4)$$

Consequently $R_t \sim \dot{M}^{-2/3}$, $R_t \sim v_\infty^{2/3}$, $R_t \sim R_*$ and $R_t \sim D^{-1/3}$.

The mass loss rate couples velocity and density field of the atmosphere because the atmosphere should be stationary and spherical Hamann & Todt (2023). It can be obtained using:

$$\dot{M} = 4\pi r^2 v(r) \rho(r), \quad (2.5)$$

where $v(r)$ is the velocity law of the wind and $\rho(r)$ is the density profile of the photosphere.

Clumping The code distinguishes between micro and macro clumping. Micro clumping is defined via the parameter *DENSCON* (D) and describes density inhomogeneities on small scales which are optically thin. It is the inverse of the filling factor and can be calculated via:

$$D = \frac{\rho_{\text{clump}}}{\langle \rho \rangle}, \quad (2.6)$$

where ρ is the density of the region. For WR stars this value is usually set between 4 and 10. Macro clumping on the other side describes large scale clumps in the wind which are optically thick (Oskinova, L. M. et al., 2007).

Chemical composition The mass fraction of atoms in a star can be changed for the following atoms: hydrogen, helium, nitrogen, carbon. The mass content of iron, nickel, chromium, cobalt, manganese, titanium, scandium and vanadium are combined under the name: *GENERIC*. The abundances of these elements in the sun were researched in Asplund et al. (2009). From there and the assumption that we have similar metallicities in the NGC 6822 as in the SMC we can scale down the abundances of the sun.

2.3 Attributes of the Wind

WR stars have strong stellar winds which are orders of magnitude higher than the solar winds. These winds can be described by their wind velocity, mass-loss rate, and clumping. It produces a typical spectral feature called P-Cygni line profile which contains an absorption part and an emission part of a line. The theoretical foundation of the stellar wind driving in O stars are presented by [Castor et al. \(1975\)](#).

The wind gets stronger with higher metallicity and thus also the wind velocity changes, too ([Crowther & Hadfield, 2006](#)). Furthermore, [Crowther \(2007\)](#) concluded in its Figure 7, that there exist a metallicity dependence of type:

$$\dot{M} = Z^m, \quad (2.7)$$

where \dot{M} is the mass loss and Z is the metallicity with $m \sim 0.8 \pm 0.2$. [Crowther \(2007\)](#) states additionally that lower metallicity environments prefer earlier WN types .

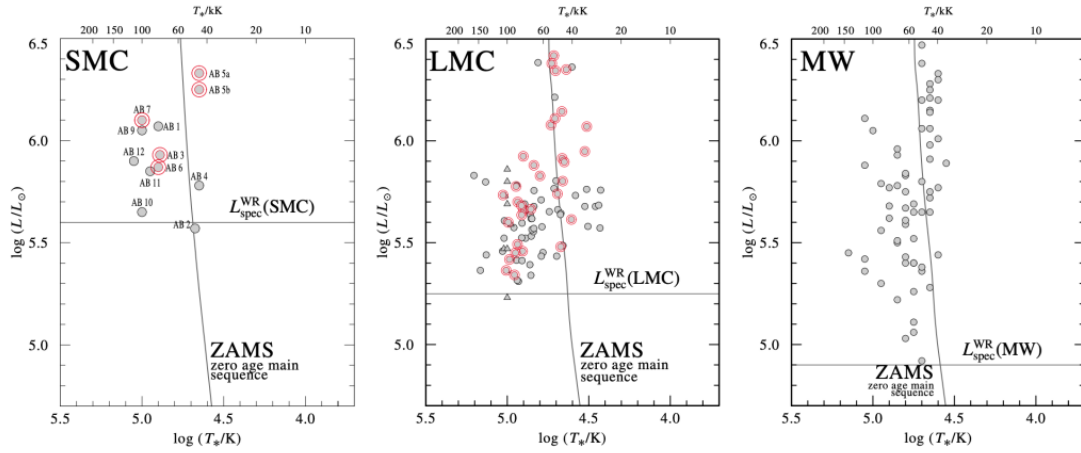
2.4 Evolutionary models

In the past, multiple approaches were developed to explain the evolution of WR stars and their observational appearance. These were expanded due to the development of modeling codes like PoWR. Nowadays, clumping is likely to have an impact on the evolution, as well as the combination of mass loss and rotation. This is needed to explain the ratio of population of WR stars relative to the population of O stars in a given galaxy. With rotation, it is possible that O stars enter earlier in the WR phase and stay longer in this stage. This single star evolutionary scenario is known as the Conti scenario (see [Conti, 1976](#); [Shenar, 2022](#))¹. The observed WN/WC ratio in a galaxy cannot be explained by only considering single star evolution (see Figure 8 in [Crowther, 2007](#); [Eldridge, J. J. & Vink, J. S., 2006](#)). Especially at low metallicity it is unclear how stars evolve to the WR stage. There close binary evolution is favored. [Shenar \(2022\)](#) summarizes the evolutionary state in Figure 2.2. [Shenar \(2022\)](#) concludes that there exists a Z dependent luminosity threshold up to which stripped stars cannot produce strong enough winds to produce a WR type spectrum. A single star in the SMC and thus similar for the NGC 6822 needs for example a mass of at least 40 M_{\odot} to be classified as a WR Star ([Shenar, 2022](#)). The initial mass corresponds to the mass the star is born with. During its life, a star loses mass because of its stellar wind. At the WR phase there is only a partial of the initial mass left.

As a last action, the WN and WC type WR stars explode in a SN type Ib/c since hydrogen and/or helium are not observed in these SN ([Woosley & Bloom, 2006](#)). Additionally, they are

¹The original reference from Conti is unfortunately unavailable for the public but the reference is seen in multiple sources.

Figure 2.2: Figure 2 from Shenar (2022), red circles are binaries. Only stars with a minimal luminosity exhibit winds to be classified as a WR star. In the SMC stripped stars need a minimal luminosity of 5.6 mag and a minimal initial mass of $\approx 40 M_{\odot}$ to be viewed as WR star.

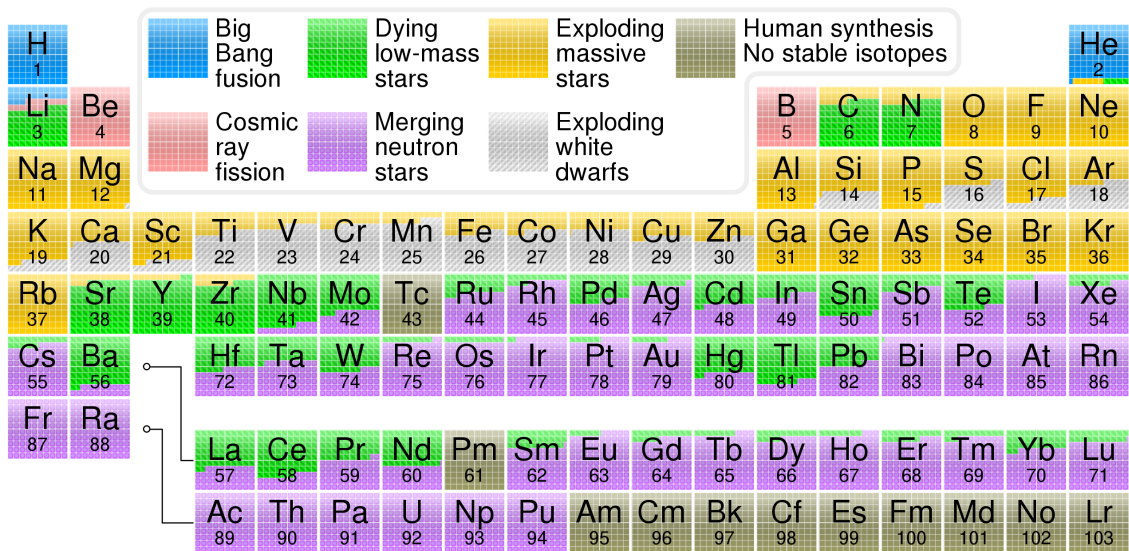


accompanied by a Gamma Ray Burst (GRB). What is left then are NSs, magnetars with a magnetic field of $\sim 10^{12} - 10^{15}$ G, or even BHs. To achieve these kinds of magnetic fields the WR star itself would need a magnetic field of $\sim 10^2 - 10^3$ G. One of the stars in this study is likely to have such a high magnetic field. Again, it is possible to reconstruct the evolution with single and with binary stars (Crowther, 2007).

2.5 Current state of research on WR stars

We know that there exist WR stars, like the former which are represented by the WNL spectral types while the later are observed as of WNE, WC and WO spectral type. Their evolution is metallicity dependent and thus is the wind. Because of our models, it is believed that they contribute a lot to the chemical enrichment in their surrounding due to rotational mixing and clumped winds. The elements which play a major role can be seen in Figure 2.3. We are dealing mostly with H, He, C, N, O, and elements in the second period. But some riddles are still unsolved. How exactly does metallicity influence the WR mass loss?; Which role has binarity for the evolution of WR stars? This study is dedicated to these open questions using a metallicity poor environment to find potential answers.

Figure 2.3: Credit: Cmglee, CC BY-SA 3.0 ([licence link](#)), via Wikimedia Commons, Data reference: Jennifer Johnson (OSU); [Nasa's astronomy picture of the day 09.08.2020](#); The periodic table shows the origin of the elements. The filling of each element represents the percentage by which element contributes to the production of this element. Among them are exploding massive stars and merging neutron stars which have WR stars as progenitors.



Chapter 3

NGC 6822 - Barnard's Galaxy

The constellation Sagittarius appears in Potsdam, all over the year, not far above the horizon. Those who, nevertheless, have the opportunity to observe the constellation, with a telescope, will discover Barnard's Galaxy (see Figure 3.1) among others. It was discovered in 1884 by the scientist after whom it was named. [De Vaucouleurs et al. \(1991\)](#), who have categorized a whole catalog of galaxies, classified NGC 6822 as type IB(s)m. This describes a barred irregular dwarf galaxy. It is part of the Local Group and is located at about 0.47 Mpc distance from the earth ([Rich et al., 2014](#)). We use their value since it is the newest researched. However, there are different distance determinations. Further methods and the comparison to LMC and SMC can be found in Table 3.1.

Figure 3.1: An [image](#) of Barnard's Galaxy ([ESO, 2009](#)). The ESO used the Wide Field Imager attached to the 2.2-metre MPG/ESO telescope at ESO's La Silla Observatory. North is upwards. The image contains B, V, R, and H-alpha filter. Its field of view is 35×34 arcmin.

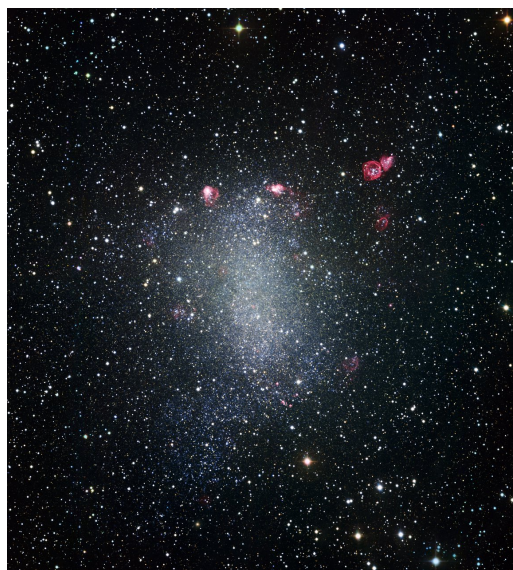


Table 3.1: Distance of NGC 6822 from different sources, in comparison with the LMC and SMC.

Reference	Method	Distance modulus (μ) [mag]	Distance [kpc]
Rich et al. (2014)	Cepheids	23.38 ± 0.06	474.241 ± 0.010
Fusco et al. (2012)	TRGB ¹	23.54 ± 0.05	510.504 ± 0.010
Musella et al. (2016) (LMC)	Cepheids	18.50 ± 0.01	50.118 ± 0.010
Marconi et al. (2017) (SMC)	Cepheids	19.01 ± 0.06	63.386 ± 0.010

¹Tip of the red-giant branch

Distance (D) and Distance Modulus (μ) are connected in the following way:

$$\mu = m - M = 5 \log_{10} \left(\frac{D[\text{pc}]}{10[\text{pc}]} \right) = 5 \log_{10} \left(\frac{D[\text{pc}]}{1[\text{pc}]} \right) - 5, \quad (3.1)$$

$$D = 10^{\frac{\mu}{5} + 1}, \quad (3.2)$$

where m is the apparent and M the absolute magnitude. Furthermore, we want to deal with the metallicity, as this has an influence on the stellar wind as we have seen in section 2.3 (see [Hainich et al., 2016](#)). The metallicity (Z) is usually defined as the total mass of all metals relative to the mass of hydrogen and helium in a region or galaxy. Another parameter which is commonly used in literature is the relative abundance of two Elements. It is defined in the following way:

$$[X/Y] [\text{dex}] = \log_{10} \left(\frac{N_X}{N_Y} \right)_* - \log_{10} \left(\frac{N_X}{N_Y} \right)_\odot [\text{dex}], \quad (3.3)$$

where X and Y are elements like, e.g. iron and hydrogen. N is the relative number density of an element. The relative abundance is given in [dex] which stands for orders of 10th magnitude (see [Maiolino & Mannucci, 2019](#)). This relative abundance can vary a lot locally, but average values can be plotted and compared with the relative abundance of the SMC and the LMC. This comparison is made in Table 3.2.

Table 3.2: Metallicity of NGC 6822 from different sources, in comparison with the LMC and SMC

Reference	Method	Fe/H [dex]
Venn et al. (2001)	A-type Supergiants	-0.49
Kirby et al. (2013)	Spectroscopy (RGB)	1.05
Sibbons et al. (2015)	Photometry C-M type AGB stars	-1.38
Tantalo et al. (2022)	C-M type AGB Stars	-1.25
Taibi et al. (2022)	Spectroscopy (RGB-Stars)	-0.89
Pilyugin (2001) (SMC)	HII regions	-0.95
Cioni (2009) (SMC)	C-M type AGB	-1.25
Taibi et al. (2022) (SMC)	Spectroscopy (RGB-Stars)	-0.94
Cioni (2009) (LMC)	RGB	-0.66
Solar	per definition	0

Since the iron abundance of NGC 6822 is similar to that of the SMC, we initially assume a metallicity like that of SMC for our stars. [Todt et al. \(2015\)](#), for instance, used $Z_{SMC} = 0.2$

Z_{\odot} to calculate grid models for the SMC. Therefore, we take the abundances from these grids for the elements Fe, N, O and C. If the reader wants to know more about metallicities in NGC 6822, please read [Taibi et al. \(2022\)](#) and [Massey et al. \(1995\)](#). [Taibi et al. \(2022\)](#) gives an iron abundance gradient in Barnard's galaxy of

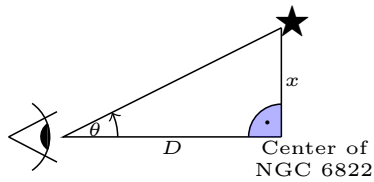
$$[\text{Fe}/\text{H}] = -(0.89 \pm 0.34) - (0.28 \pm 0.08)R, \quad (3.4)$$

where R is the deprojected radius from the center of the galaxy in kpc. In Figure 3.3, one can see the location of stars we selected for this research with respect to the galactic center. By using SAOds9 it is possible to obtain the distance to the galactic center in arc minutes. To convert this value into parsec, one can use the following expression:

$$\tan(\theta) = \frac{x}{D} \quad (3.5)$$

where x is the distance of two sources in the universe, D is the distance from us to these two sources and θ is the angle in degrees from one source to the other, as seen from earth.

Figure 3.2: Schematic explanation of angular distance. We assume a right angular triangle for this problem with the geometrical advantage to use formula 3.5. The black star represents a target stars. The eye represents the observer on earth.



A better explanation gives Figure 3.2. The calculated values as well as their iron abundance can be seen in Table 3.3. On its way to us, the light is absorbed by dust and deflected or emitted in different directions. This causes the light to lose energy and the object to appear dimmer and redder than it actually is. This is called extinction and reddening, respectively. The reddening in NGC 6822 changes with distance from the galactic center (0.45 mag) to the outermost regions (0.25 mag) ([Massey et al., 1995](#)). [Schlafly & Finkbeiner \(2011\)](#) found that the mean reddening along the line of sight to be $E(B-V) = (0.2028 \pm 0.0098)$ mag. NGC 6822 moves with a heliocentric velocity of (-54.86 ± 2.1) $\text{km} \cdot \text{s}^{-1}$ ([Namumba et al., 2017](#)). It is a negative velocity because it is moving towards us. Therefore, we can conclude that our spectra are blue-shifted.

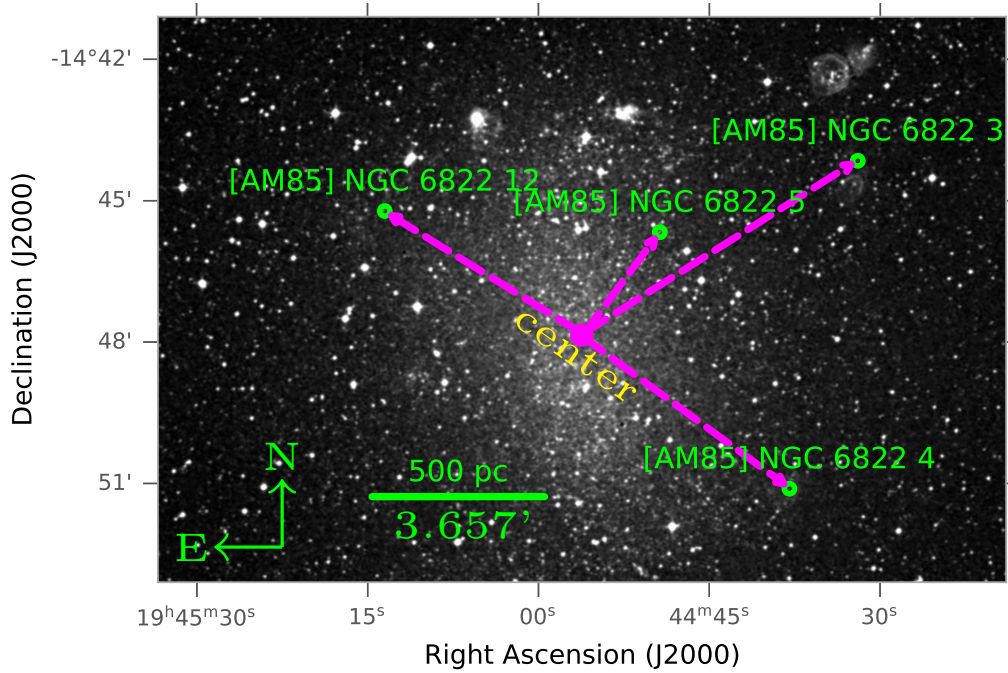
Besides, to our observed stars, NGC 6822 has some other interesting objects. Among them are some star forming regions, molecular clouds and H II regions which are marked in Figure 4.3. Because of these young regions, the low metallicity and the amount of massive stars, it is a sought-after observational object.

In its center, Barnard's galaxy has a bright point size X-ray source. It is assumed to be a black hole binary system ([Eskridge & Raymond E. \(1997\)](#)).

Table 3.3: Distance from the center of Barnard's galaxy to the target objects with the calculated iron abundance from equation 3.4. The errors which could occur here are mainly human made and cannot really be estimated. Furthermore, these should be seen as minimal values since in formula 3.4, R is the deprojected radius whereas we could only use a projected radius in SAODs9.

Star name	distance [arcmin]	distance [pc]	[Fe/H] [dex]
[AM85] NGC6822 3	4.913	670	-1.15
[AM85] NGC6822 4	2.72	372	-1.10
[AM85] NGC6822 5	5.51	753	-0.99
[AM85] NGC6822 12	6.90	944	-1.08

Figure 3.3: This is an image from NGC 6822, made via the help of [hips2fits \(Université de Strasbourg/CNRS, 2023\)](#). It is a combined image, of DSS red and DSS blue, in grey scale. The green circles mark our sample of WR stars. The middle magenta circle marks the center. The length of the magenta arrows indicate the projected distance from the center to the star. These distances are written in Table 3.3.

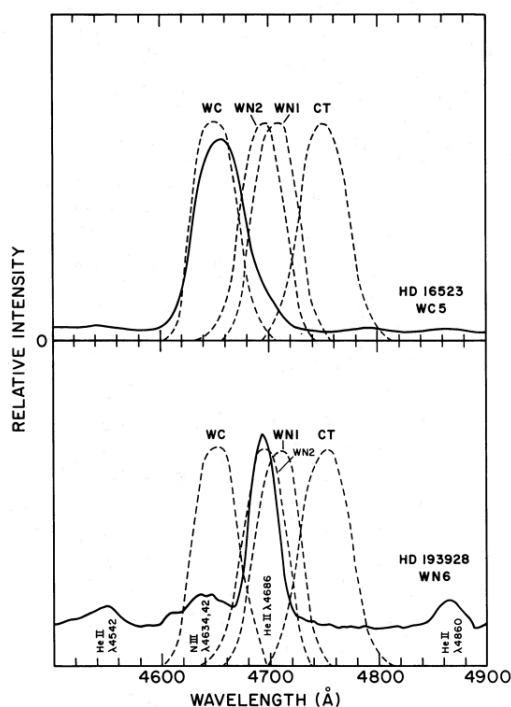


Observations

The first difficulty one encounters when studying WR stars is finding them. Afterwards, follows the challenge of observation. Both photometric and spectroscopic data must be reduced and extracted to eliminate and/or reduce known sources of error. A comparison with the photometry from the literature is necessary to find the luminosity of the star. However, literature and observation can vary, and it is worthwhile to independently calculate the photometry using the corresponding HST images. The whole area, for which we applied observation time, can be seen in Figure 4.3.

4.1 Methods to detect WR stars

Figure 4.1: Filter system to find WR stars as in [Armandroff & Massey \(1985\)](#).



There are several ways to find WR stars. Their emission lines make them easy to distinguish from other stars which have absorption spectra, usually. Nebulae can also appear via emission lines, but these are narrower than those of WR stars. [Armandroff & Massey \(1985\)](#) give multiple examples on how to find WR stars:

- a) low dispersion objective-prism techniques,
- b) interference-filter photography,
- c) spectroscopy in selected regions.

[Armandroff & Massey \(1985\)](#) performed interference-filter photography, by using a charge-coupled device (CCD) with a set of 50 Å-wide interference filters with optimal central wave-

length to detect WR stars in NGC6822. These optimal wavelengths are at lines typical for WC and WN stars (see Figure 4.1). The WC filter was set to $\lambda_{\text{central}} = 4649 \text{ \AA}$ and is sensitive to the emission line C III $\lambda 4650 \text{ \AA}$. There are two WN filters located at $\lambda_{\text{central}_1} = 4706 \text{ \AA}$ and $\lambda_{\text{central}_2} = 4693 \text{ \AA}$ specifying the WN type. Additionally, there is a continuum filter to distinguish between the WC and WN type. The WN filter identifies WC stars too, since both contain He II $\lambda 4686 \text{ \AA}$. A comparison with the continuum filter clarifies the classification.

4.2 Our observation of the four WR stars

We applied for observing time at the VLT for long slit spectroscopy in the field which can be seen in Figure 4.3. We gave the coordinates of the four possible WR stars from [Armandroff & Massey \(1985\)](#). Because of their distance from earth and low apparent magnitude ($V \sim 20$) mag, one needs a telescope of a corresponding size to be able to capture enough of their light. This is what the Paranal unit telescope mirror offers with its 8.2 diameter cassegrain telescope.

The spectrograph used was FORS 2 ([Appenzeller et al., 1998](#)) (see Figure 4.2). This has the possibility to record spectra of one or more objects simultaneously and to determine the polarization of the light. The camera of the telescope contains two CCDs covering the area around the star. The desired object is located in only one of them. From each CCD we received one spectrum in the visual blue and one in the visual red. Each observation was conducted twice. In the end, we analyzed 32(+8) observations. The 8 additional pictures were needed because the observers made an error in one observational run. Tables (6-25), in the appendix, contain all information about the datasets: when they were taken and what is contained.

By using different grating prisms (grisms), wavelengths between $\lambda 3300 \text{ \AA}$ and $\lambda 11000 \text{ \AA}$ can be achieved with a spectral resolution (R) between 260 and 2600. The grisms used, and their properties, can be found in the Table 4.1. Finally, we obtain usable spectra in the optical range between $\lambda 4625 \text{ \AA}$ and $\lambda 7149 \text{ \AA}$. The central wavelength is at $\lambda_c = 5203 \text{ \AA}$ with a resolution of $R=2100$. At this wavelength we are able to distinguish lines with a:

$$\Delta\lambda = \frac{\lambda}{R} = 2.48 \text{ \AA}. \quad (4.1)$$

Figure 4.2: The [image](#) shows FORS (yellow), mounted at the Cassegrain focus of the Unit telescope 1 ([ESO, 1998](#)).

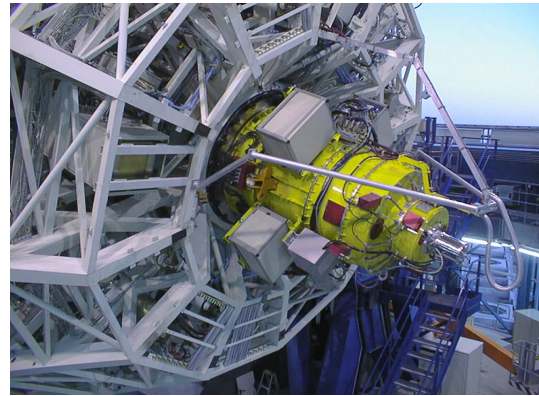


Table 4.1: Used gratings with their spectral resolution (R)

grism	$\lambda_{central}$ [Å]	λ_{range} [Å]	dispersion [Å/mm]/[Å/px]	R at $\lambda_{central}$ [Å]	R at $\lambda_{central}$ with 0"3 [Å]	additional filter
GRIS_1400V+18 (3,5)	5203	4560 - 5860	20.8/0.31	2100	5660	-
GRIS_1200R+93 (5)	6530	5750 - 7310	25.0/0.38	2140	5330	GG435+81

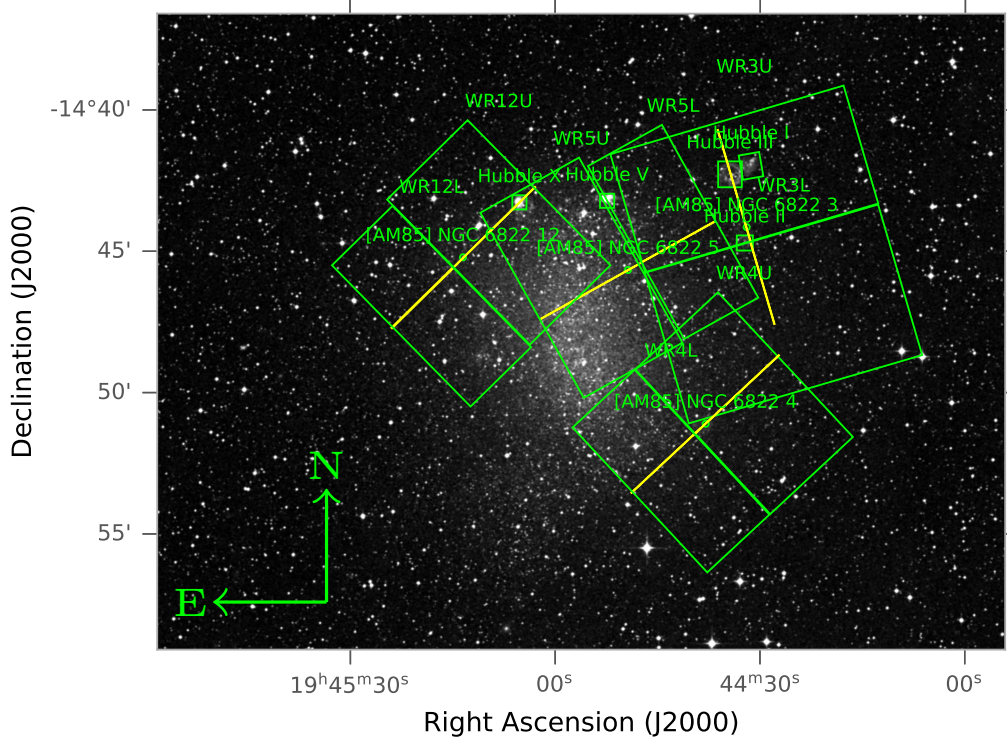
Long Slit Spectroscopy (LSS) and CCD cameras Among multiple methods, long slit spectroscopy measures not only the flux of one point source but multiple objects which are additionally observed within the slit. The resolution and signal-to-noise ratio (SNR) of the observed spectra was previously determined from calculated model spectra to ensure that we get sufficiently detailed information about the stars. A minimum acquisition time of 2800 s and a seeing of the full width half maximum (FWHM) of 0.8" were determined to achieve a SNR of 30. It allows us to find a good fitting model from which we then conclude parameters like luminosity, rotation and temperature from the star. We use the high resolution collimator which has a pixel scale of 0.125" per pixel. This gives a field size of 4.25' \times 4.25'.

FORS2 has two detector systems. One consisting of two 2kx4k MIT CCDs (15 μ m pixels) and one consisting of two 2kx4k E2V CCDs (15 μ m pixels). Furthermore, we use LSS with a slit width of 0.5". Stars up to a magnitude of 24.2-23.3 mag can be observed.

The resolution and other aspects of the used gratings can be seen in Table 4.1. The filter GG435+81 is intended as an order separation filter for spectroscopy. All information about the hardware can be found on the [FORS2 ESO webpage](#) or in the [FORS2 user manual](#), (see [ESO, 2022, 2023](#)).

Control the data After each observation was conducted, we assured that there was no problem with the data. We opened the acquisition images, the science images and the slit images in an rgb image with SAOds9. Additionally, we plotted circles on the position of our target stars. By doing so, we checked if the slit lies on our target objects. During the process, we detected that the telescope missed one of our target stars. This can be seen in Figure 4.4. We asked for re-observation and received the data some weeks later. With the assurance that the data was ok, we proceeded with the data reduction.

Figure 4.3: This is an image from NGC6822, made via the help of [hips2fits](#). It is a combined image, of DSS red and DSS blue, in Grey scale. The green squares mark the CCD field of views + interesting He II regions (Hubble I,II,III,V,X). Our four target stars are marked with green circles. The slit position is marked in yellow. We have spectra from all regions which sit on the yellow slit position. WR+Number+U/L is an abbreviation used during the work progress to name the different CCDs.

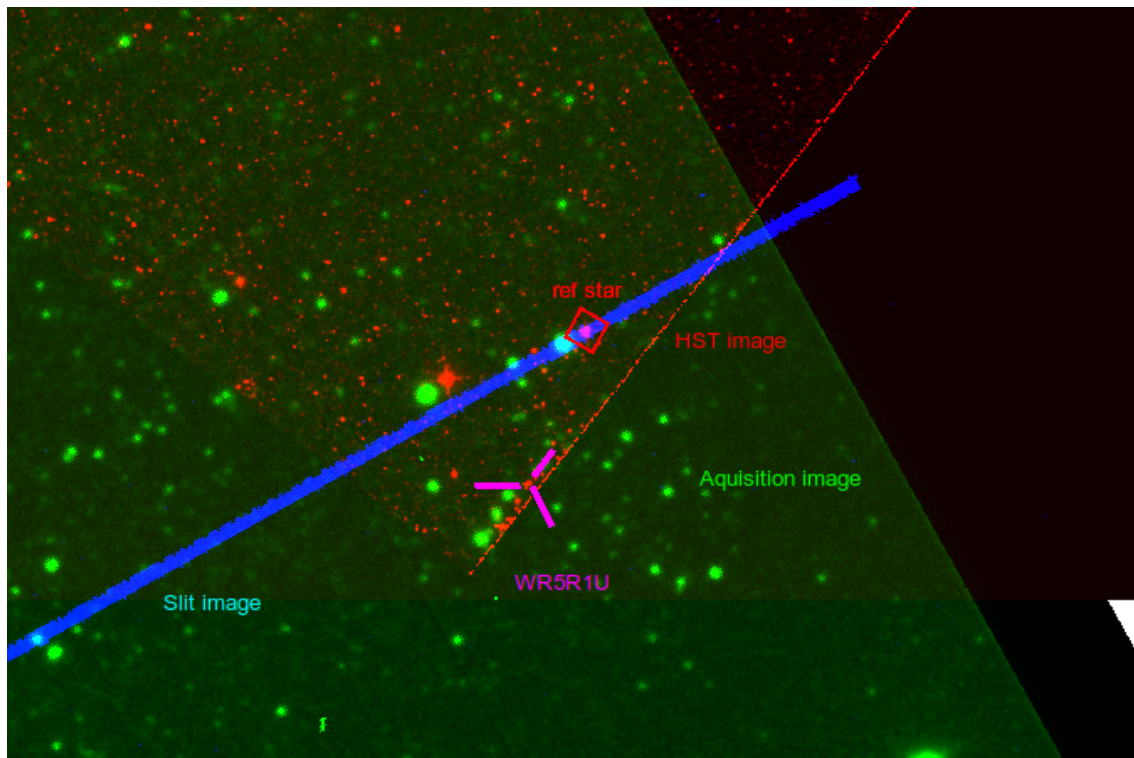


4.3 Reduction and extraction with Esoreflex

Esoreflex is a program especially written for analyzing science data from ESO VLT ([Freudling et al., 2013](#)). With *Esoreflex*, it is possible to reduce and extract spectra from multiple files and objects within hours, whereas a reduction and extraction with *IRAF* would take days or months for the same amount of data. This is its great advantage and the primary reason why we used it for this work. The pipeline contains multiple workflows for the different instruments mounted on the VLT. We worked with the pipeline for the FORS 2 instrument, [source kit 5.6.2](#). The data organization is described in the Appendix (see Table 5).

After installing and opening *Esoreflex*, we changed the path for *RAW_DATA_DIR* and *CALIB_DATA_DIR* to the path where we saved the science data from the telescope. The startup window for the workflow can be seen in Figure 4.6. Since the program uses the fits header from each file to detect its purpose, i.e. science image, acquisition image, calibration images, dark and flat frames of stars and grisms, there is no need for structuring the data in more detail. The reduction of all images can now be proceeded and is mostly done with the default parameters.

Figure 4.4: The wrong slit position on [AM85] NGC6822 5. **Green**: acquisition image, **red**: HST image, **Blue**: Slit position. Also marked in a **red square** is the reference star. With the **violet lines** the position of the WR star is indicated. Because of multiple reasons, acquisition image and HST image object position differ slightly from one another.



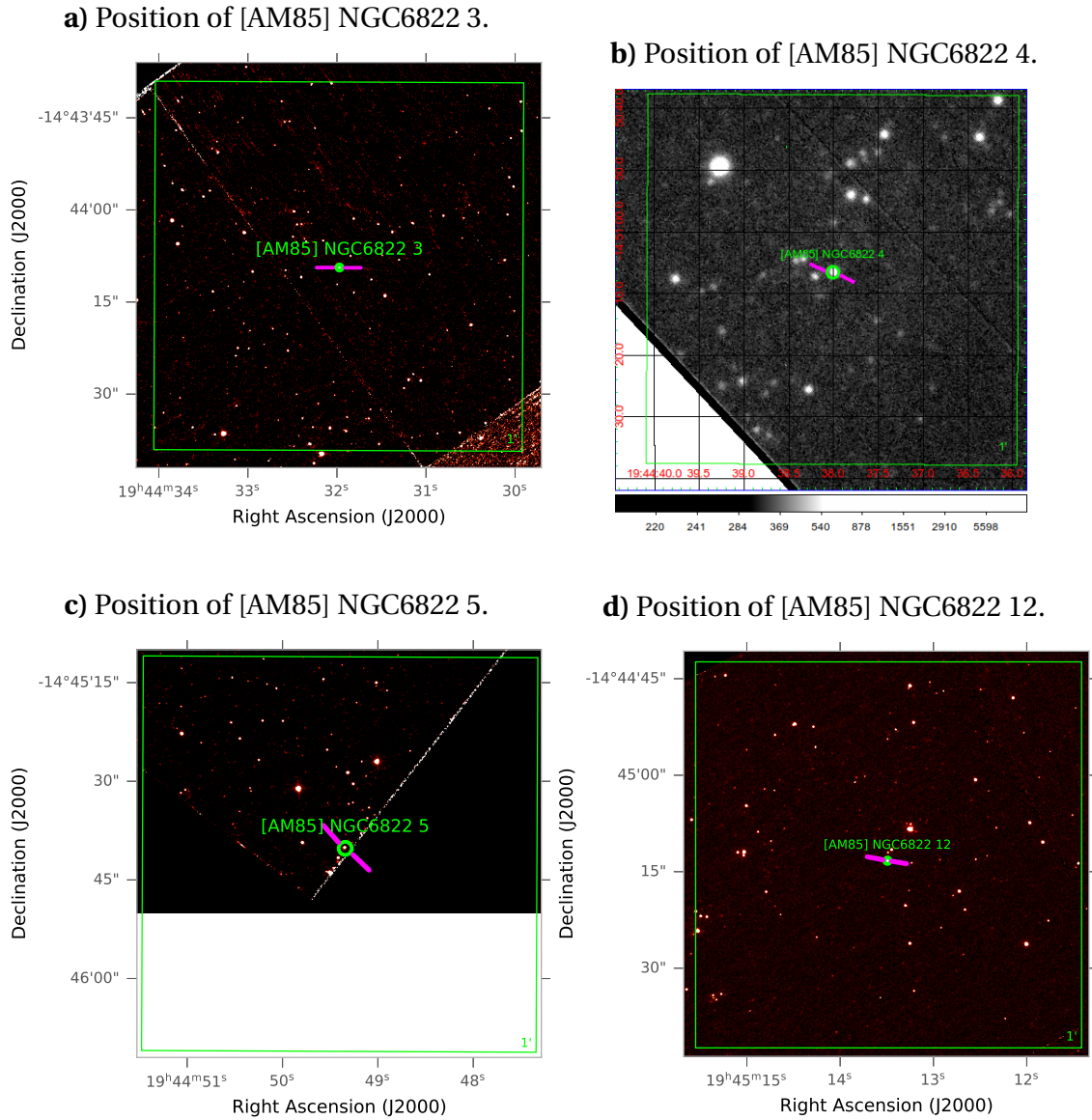
Only in some cases it was necessary to change some parameters since error parameters were out of boundaries which were given in the manual. Affected data can be seen in the appendix.

Furthermore, we subtract the sky from the images to reduce atmospheric effects. Sky subtraction in `Esoreflex` has three options (methods) to choose from.

- sky global,
- sky local,
- sky median.

Sky global is used for big sources like nebula or star forming regions. Here the continuum of the hole slit is used to subtract the source. Sky local is utilized when working with point-like sources, as it specifically involves subtracting the sky background within the immediate vicinity of the point-source. Sky median is used for curved slit, since here the subtraction is done after reducing the image instead of before as in the other two options. The third option is not used because we do not look at objects which are at the curve of the slit. Furthermore, when we checked how much of the data points are reduced by this mode, it was clear that it subtracts too much real data. In the end, we reduced every science data with both, once with

Figure 4.5: Positions of our sample of WR stars. North is upwards, east is to the left side in every picture. Only [AM85] NGC6822 4 is not an HST image but the acquisition image from the VLT. Each green square has the size of one arc-minute which correspond to length of 137 pc. One can compare it with the Figure 5 in [Armandroff & Massey \(1985\)](#).



sky local and once with sky global to have the opportunity to select the correct subtraction for every source.

The output files are .fits files, containing the spectra of all identified sources. We have one file for each object. The sources for the spectral output were identified by the pipeline itself. It uses a threshold to distinct spectra from background noise. Additionally, it produces a file containing coordinates connected to the spectra of every object. Because this object table is inconvenient to read, we wrote a Python script which extracts all important data in a more suitable format.

By comparing the coordinates of the spectra with the coordinates with our target star via SAODs9, one can select the file containing the spectra of the desired star. Another self-written python script extracts the data in a xy table format in a .dat file. This will be saved in the target star folder.

For the main sample stars we have two spectra for the red and the violet part of the visible spectrum. These are merged using WRplot.

Afterwards, we normalize the spectrum by dividing the spectra through a cubic spline interpolation. The points to create this function were set by hand in the merged spectrum plot. Now the normalized spectrum can be plotted with WRplot. A detailed description on every script, its position and usage is explained in the appendix.

4.4 Photometry

Photometry is needed to examine the luminosity of an object. It represents how many photons are detected in a defined time interval per wavelength. In the history of photometry there were different photometric systems. We will use the photometry to adjust the SED of the spectrum to the right luminosity.

Johnson's photometric system

This photometric system was introduced by [Johnson & Morgan \(1951\)](#) and is still used today. It is divided into a (U) filter, a Blue (B) filter and a Visual (V) filter. Their corresponding wavelength at which these filters respond the most are at 3630Å, 4257Å and 5292Å, respectively ([Johnson & Morgan, 1951](#)). Later it was expanded to red and infrared wavelengths to deal with cooler stars, too. Since WR stars are hot stars, and emit the strongest in the UV, the UBV system is sufficient for this thesis. By calculating $(U - B)$ and $(B - V)$, it is possible to make a color-color diagram ($(U - B)$ to $(B - V)$ diagram). To compare values from different stars, a $(B - V)_0$ and a

$(U - B)_0$ value were introduced respectively, such that for A0 main sequence Stars

$$(B - V) - (B - V)_0 = 0, \quad (4.2)$$

$$(U - B) - (U - B)_0 = 0. \quad (4.3)$$

From the color-color diagram, one can deduce the temperature of the star as well as the evolutionary stage. Furthermore, it is possible to get reddening and extinction values. [Massey et al. \(2007\)](#) applied the Johnson photometry, among others, for stars in the NGC6822.

Reddening and extinction

All information in this subsection is taken from Swinburne University of Technology (see their [website](#)) ([Swinburne University of Technology, 2023](#)). Knowing the UBV Photometry of an Object one can calculate the reddening by:

$$E(B - V) = (B - V) - (B - V)_0. \quad (4.4)$$

Reddening and extinction are linked through:

$$A_V = 3.2 \cdot E(B - V), \quad (4.5)$$

where A_V is the extinction in the visual. From there it is possible to calculate the distance via the magnitude-distance law:

$$d [pc] = 10^{0.2(m - M + 5 - A_V)}, \quad (4.6)$$

where m is the apparent magnitude and M the absolute magnitude. We get reddening and extinction from aligning a model to the photometry, such that we do not need to calculate $(B - V)$ values.

HST Photometry

There are a lot of sources from which one could obtain the photometry of an object. But many references have limited explanations as to how they obtain them. Furthermore, it turns out that the photometry from Johnson and the ones obtained from online sources¹ is not true i.e. does not fit at all to my observations. [Bianchi et al. \(2001\)](#) used HST WFPC2 photometry with F225W, F336W, F439W and F555W filters for [AM85] NGC6822 12 where their values fit quite well to the observation.

¹Obtained with the programs `DAOphot` and `SExtractor` from HST images given in online catalog: see MAST archive.

The conclusion for us was, nevertheless, to independently extract the photometry from the corresponding HST images. For this, we used IRAF. The HST images are from 2009, so they are newer than any previously used to determine photometry from the selected sample. The fits file images are downloaded from MAST archive. We will use the IRAF / APPHOT procedure. The HST images use the ST-system for the Zero Point (ZP). There are two other systems, the Vega and the AB system. Further reading about these systems and ZPs can be done in the HST [user documentation](#) (Space Telescope Science Institute, 2022) or in Koornneef et al. (1986).

IRAF IRAF is a powerful program for data analysis in Astrophysics and Astronomy (Tody, 1986, 1993). Our goal is a value for the magnitude of an object (later referred to as STMag). This can be obtained in multiple ways in IRAF. With the command `imexamine`, it is possible to obtain a first draft of the photometry. But since this is only a reference value for a quick look, it should not be used scientifically. For the scientific value we use `DAOPHOT` and follow the steps given in these manuals (Davis, 1994; Massey & Davis, 1992).

Calculating physical flux density For the SED, one needs to find the flux density. From the HST images we obtain a photon count which can be converted into flux using:

$$STMag = -2.5 \cdot \log_{10}(F_{\lambda}) - 21.10, \quad (4.7)$$

where STMag is the magnitude of an object whereas F_{λ} in [$\text{erg cm}^{-2} \text{ \AA}^{-1} \text{ s}^{-1}$] is the flux density (see Space Telescope Science Institute, 2022). The ZP can be obtained from the fits header or via

$$ZP_{ST} = -2.5 \cdot \log_{10}(PHOTFLAM) - 21.10, \quad (4.8)$$

where *PHOTFLAM* is given in units of [$\text{erg cm}^{-2} \text{ \AA}^{-1} \text{ electron}^{-1}$]. *PHOTFLAM* is a scaling factor between an instrumental flux in units of electrons per second and a physical flux density. This value is written in the fits header. The STMag from IRAF needs to be corrected by the ZP magnitude of the ST-system. All these values are now used in the `WRplot` script to calculate the physically relevant flux density. By transforming Equation 4.7, one gets for the flux density:

$$-2.5 \cdot \log_{10}(F_{\lambda}) = STMag + 21.10, \quad (4.9)$$

$$\log_{10}(F_{\lambda}) = -\frac{STMag + 21.10}{2.5}. \quad (4.10)$$

The reader might be confused about different values on different web pages or by taking a more detailed look into the `WRplot` script. There, 10^{-ZP} is often used which has to be converted backwards again with $\log_{10}(10^{-ZP})$ to get the real ZP value.

IRAF assumes a ZP of 25. Because our calculated ZP for each HST image differs from 25, we need to subtract our ZP from 25 and correct the Value which we got from IRAF. The following values can be studied in the corresponding section for each star (See Tables: 5.1, 5.3, 5.6).

Figure 4.6: The ESOREFLEX starting window for FORS workflow. Under setup directories one needs to change the path to where the data is located. On the bottom one can see a flowchart of the program.

The screenshot displays the ESOREFLEX starting window for the FORS workflow. The window title is "File:/home/julian/Dokumente/Masterche...kflows/fors-5.6.2/fors_spec_mypath.xml". The main content area is titled "FORS Workflow For Spectroscopy Data (v. 5.6.2)".

The window is divided into three main sections:

- Workflow Instructions:** Contains instructions on how to run the workflow on demo data or different data sets, including steps like "Turn on highlighting", "Click on RAW_DATA_DIR", and "Press the Run button".
- Setup Directories:** Lists input and output directories, such as ROOT_DATA_DIR, RAW_DATA_DIR, CALIB_DATA_DIR, END_PRODUCTS_DIR, and WORKING_DIRECTORIES.
- Global Parameters:** Lists various parameters like RecipeName, ErrorDir, WFS_IMAGE, GlobalParameter, and ProductName, with brief descriptions of their functions.

Below these sections is a flowchart illustrating the workflow steps:

- Step 1: Data Organisation and Selection:** Includes actions like "Insert primary and secondary", "Data Selection", and "Data Reduction".
- Step 2: Creation of Master Calibration Files:** Includes the "MasterCal" action.
- Step 3: Response computation:** Includes the "Response" action.
- Step 4: Science Reduction:** Includes the "Science" action.
- Step 5: Output Organisation:** Includes the "Output" and "ProductViewer" actions.

The bottom of the window shows auxiliary and debug parameters, including GLOBAL_TIMESTAMP, ESOREFLEX_DEBUG, END_PRODUCTS_SUBDIR, and FILE_SELECTED.

Spectral analysis and comparison with the model

We present a spectral library of our target stars (see Figure 4.5). Afterwards, we will take a detailed look at the spectra of [AM85] NGC6822 12. The other stars and their major features will be only shortly mentioned.

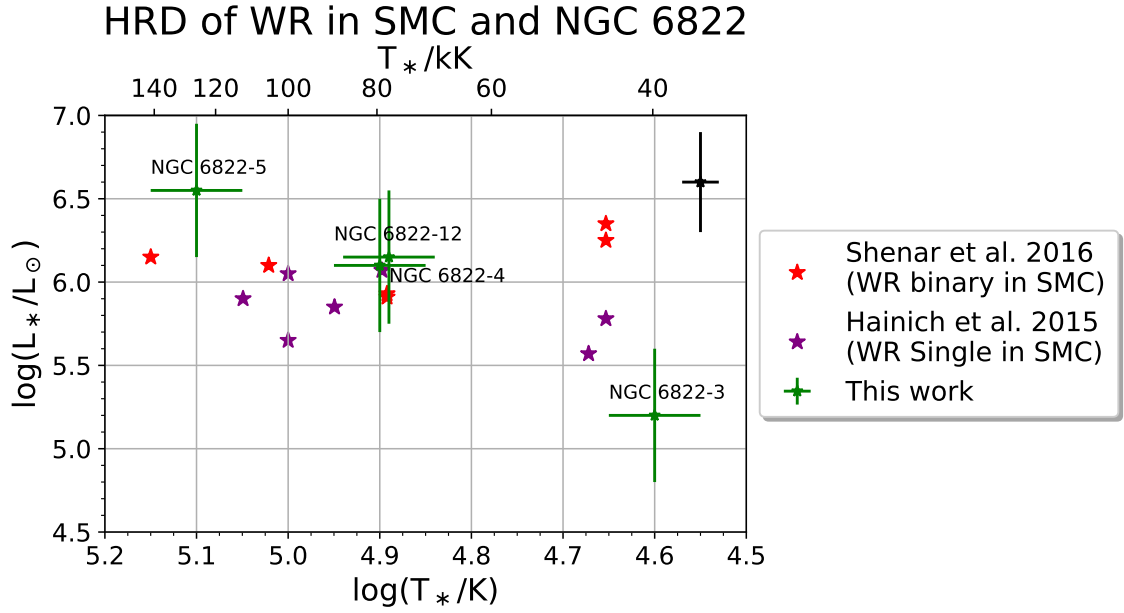
5.1 Spectral library of WR Stars in NGC 6822

The spectra of the four WR stars and their SEDs are shown on the following pages (see Figure 5.2-5.5). The blue curve always represents the collected data whereas the red curve shows the modeled spectrum. For the star [AM85] NGC6822 12 we spent a lot of time to find a more suitable model than was previously calculated with the grid models. These three other stars are only plotted with their best comparable model grid spectrum. With a first approach using the χ^2 method and comparing it afterwards with the models around the grid model by eye it was possible to find the best fitting grid model for each of these stars. The grid models can be found on the [website](#)¹ of the massive star research group in Potsdam (Hamann et al., 2016). More information about the script and other python scripts used can be found in the Appendix.

All stars are put into a HRD and compared with studies of WR stars in the SMC in Figure 5.1.

¹Link in the appendix.

Figure 5.1: HRD of our sample of stars compared with the sample of WR stars from the SMC from Hainich et al. (2015) and Shenar et al. (2016). Black errorbars indicate the errors from the literature.



5.2 In depth analysis of [AM85] NGC6822 12

This star is the first of the four which we have analyzed. The object is located at RA (J2000) 19:45:13.47 and Dec (J2000) -14:45:12.3. It was first discovered by Westerlund et al. (1983) and classified as a WN3 star. Two years later, it was re-observed by Armandroff & Massey (1985) and classified as a single WNE star. Bianchi et al. (2001) did an analysis of massive stars in the NGC 6822 and serendipitously² obtained a spectrum of that star³. They concluded that it is a WN3(-4) type without hydrogen. Their temperature estimate of 38 kK was obtained from photometry.

Photometry

There are multiple sources for the photometry which did not make sense in comparison with the SED fit (see Figure 5.6). The HST file names which we used to get the photometry from, use the following pattern:

hst_08675_36_wfpc2_\$filename_wf;

where \$filename is the filter name from Table 5.1.

²not actively searching for explicitly WR stars or this star in particular.

³It is called LB-f2-75 in their paper.

Figure 5.2: Spectrum of [AM85] NGC6822 12: green boxes indicate Photometry by Bianchi et al. (2001), blue boxes indicate photometry extracted by IRAF with DAOPHOT. Black shows the observed spectrum, red the model spectrum. Blue is the normalized observed spectrum.

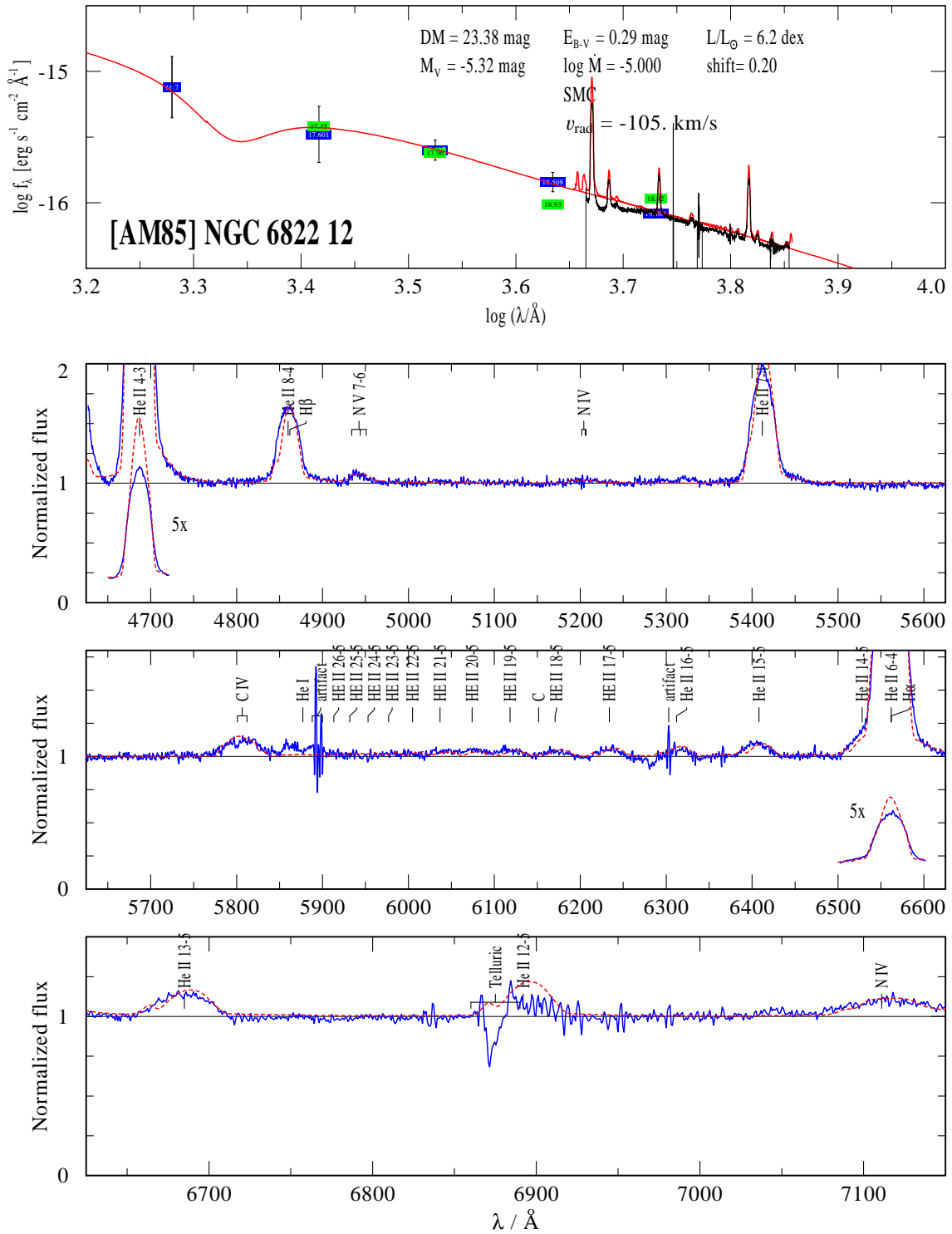


Figure 5.3: Spectrum of [AM85] NGC6822 5: Black shows the observed spectrum, blue is the normalized Spectrum, red is the model spectrum.

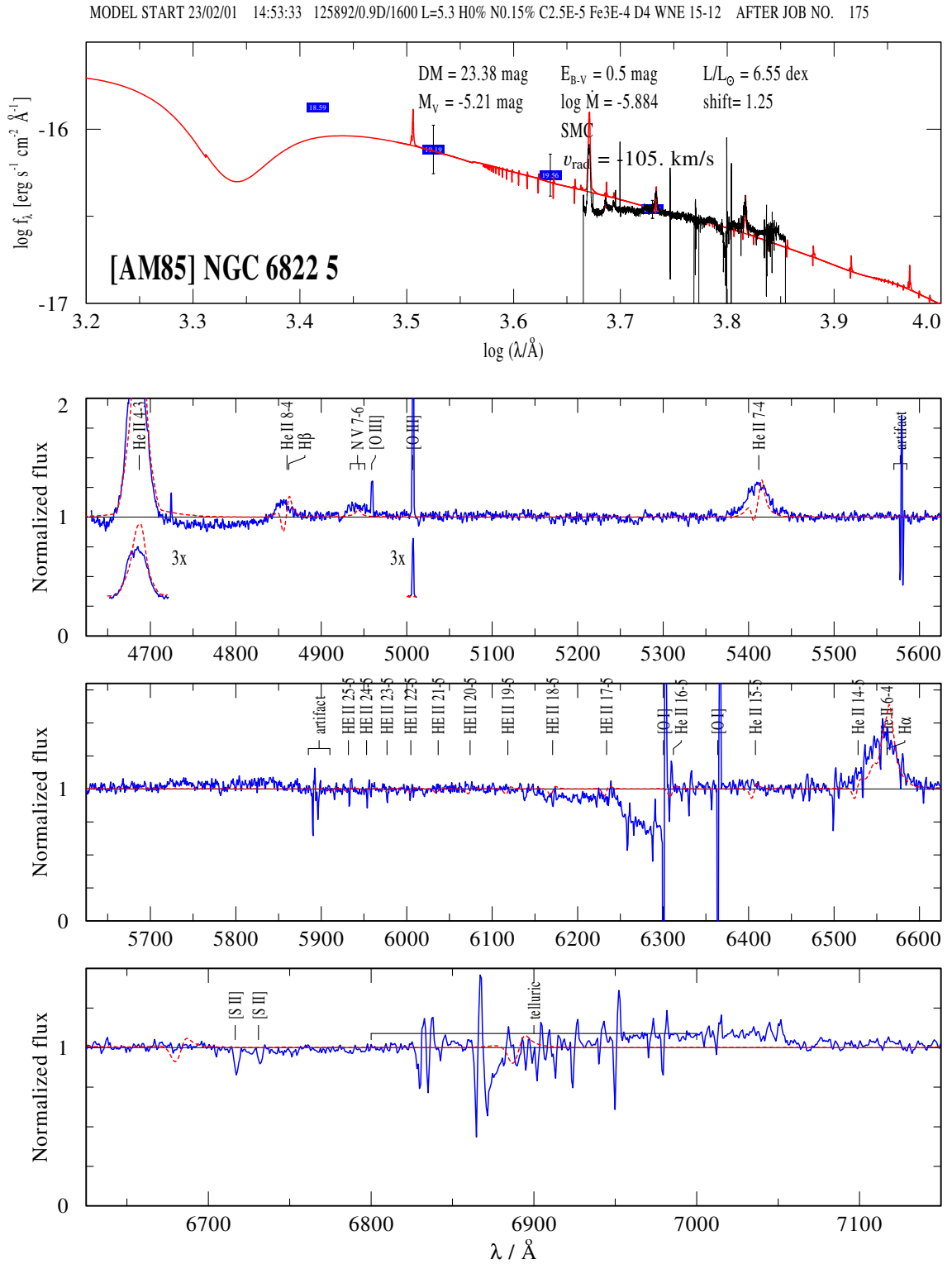


Figure 5.4: Spectrum of [AM85] NGC6822 4: Black shows the observed spectrum, blue is the normalized Spectrum, red is the model spectrum.

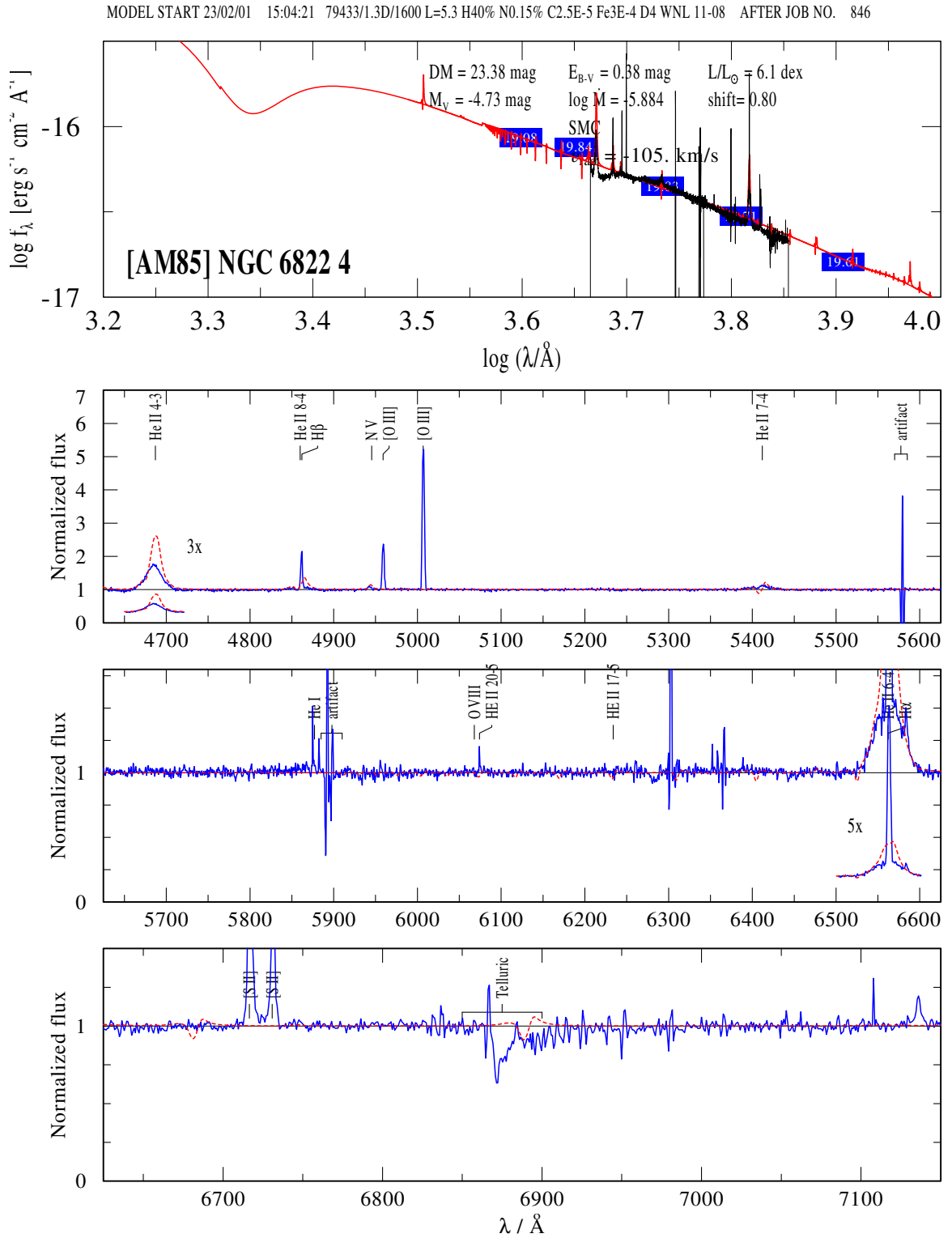


Figure 5.5: Spectrum of [AM85] NGC6822 5: Black shows the observed spectrum, blue is the normalized Spectrum, red is the model spectrum.

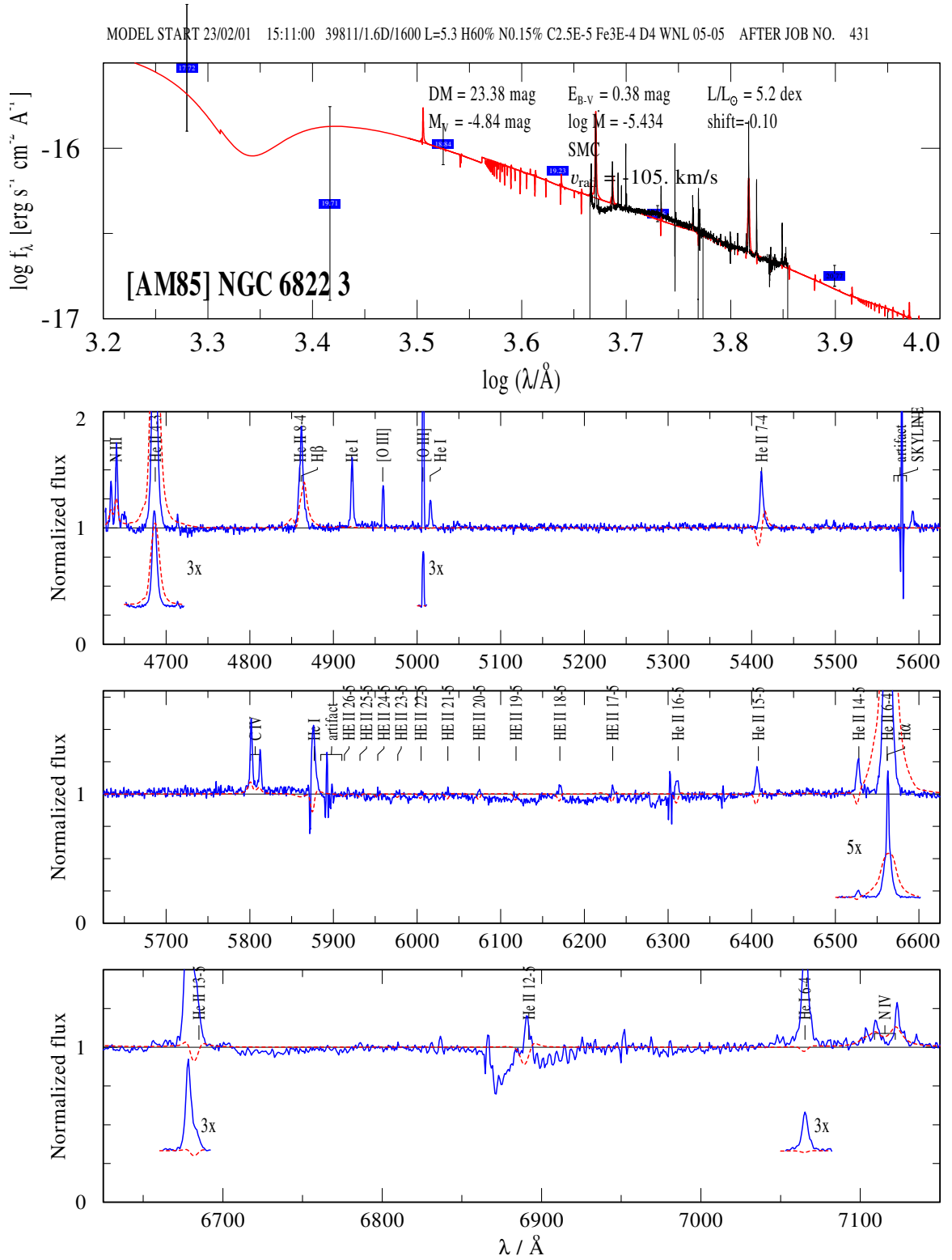


Figure 5.6: A SED with a Model for [AM85] NGC6822 12 with all possible photometric values. The colors stand for: Sextractor ST-system (yellow color), Sextractor VEGA-system, DAOPHOT ST-system, DAOPHOT VEGA-system, Johnson, IRAF, Bianci with numbers.

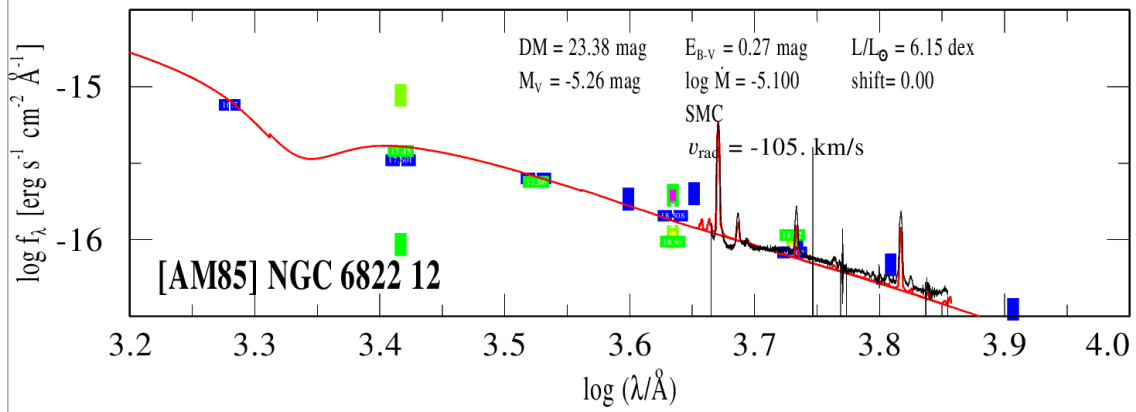


Table 5.1: Photometry of [AM85] NGC6822 12 obtained with DAOPHOT.

Filter	f170w	f225w	f336w	f439w	f555w
Apperent magnitude (mag)	16.700	17.601	17.879	18.508	19.108
Uncertainty (mag)	0.583	0.535	0.192	0.184	0.084
Date (dd.mm.yyyy)	10.11.2009	10.11.2009	10.11.2009	10.11.2009	10.11.2009

Finally, we extracted the photometry from the HST images with the DAOPHOT task in IRAF. The results and images we used are listed in Table 5.1.

Spectroscopy

In Figure 5.2, one can study the spectrum of [AM85] NGC6822 12 in detail. We obtain a Doppler shift of (-50 ± 5) km/s for the star by adjusting the model to the observation by eye. The observed spectrum is corrected by this factor. The spectrum of the violet region starts at $\lambda 4625.6 \text{ \AA}$ and ends at $\lambda 5934.4 \text{ \AA}$. The red spectrum is seen between $\lambda 5871.22 \text{ \AA}$ and $\lambda 7194.54 \text{ \AA}$. The spectrum shown is a composite of all lines, fitting best to the observation. While searching for the best fitting model, we were able to fit some lines better, while others matched the observation worse than in this spectrum shown. In the following paragraphs, the most prominent features of this spectrum are explained in detail.

He II at $\lambda 4868 \text{ \AA}$ This line is too strong in all calculated spectra where most of the other lines fit. If this line matches the observation, all other lines are too weak.

He II/H β versus He II at $\lambda 5411 \text{ \AA}$ These two lines are a good indicator whether the star contains hydrogen and if it does, then how much. If we add up to 10% hydrogen to the model, these

lines would have the same height. Thus, we conclude, if this star contains hydrogen, then only less than 10%. In combination with the $H\alpha$ line at $\lambda 6560 \text{ \AA}$ this value can be corrected to even less than 5% hydrogen since the $H\alpha$ line would be too strong otherwise. Because all the wind lines are broader than the difference between the wavelength difference between He II and its Balmer Series companions from the hydrogen atom, both, hydrogen and helium are contributing to the line shape. It is thus difficult to say to which extent which element is contained in that line.

The He II Pfund-Series From $\lambda 5910 \text{ \AA}$ to $\lambda 6900 \text{ \AA}$ the reader can see the He II cascade to the fifth shell. This is called the Pfund Series, which was explored by [Pfund \(1924\)](#). Strictly speaking, it applies only to the hydrogen atom, but can be extended to hydrogen-like elements such as He II. To have a 20th shell, the Atom needs enough free space around it to capture or maintain the excited electron. In conclusion, this leads to a low density i.e. high mean free path value at the position where these photons are emitted.

Abundances: C IV, N IV and N V The more massive elements also react to the wind parameters. Where the wind lines of an element are strongest and weakest, depending on the distance to the stellar center, can be studied on the [web pages](#) of the massive star research group in Potsdam. Through these elements, one can also check the abundances. Since the oxygen content in the galaxy is about the same as in the LMC, we could assume that the C-N-O cycle of the stars is also different from NGC6822. However, if we change the abundances of N and C to the ones used for the LMC grids, it becomes clear that the nitrogen and carbon lines become too strong.

Spectral range $\lambda\lambda(5850 - 5950) \text{ \AA}$ In the superimposed area of the two spectra, i.e. at their respective ends, effects occur that are due to the reduction and the instrument. Such artifacts can be seen, for example, in the sodium lines around $\lambda 5900 \text{ \AA}$. In [Bianchi et al. \(2001\)](#) the small emission bump at $\lambda 5850 \text{ \AA}$ is interpreted as a He I line. This can help to determine the temperature of the star. If a marker is placed at the He I line, it can be seen that the bump appears strongly blue-shifted relative to the marker, although the spectrum has already been corrected for the Doppler effect. It is possible that the He I line is strongly broadened and overlaps with the sodium lines, or that it is not He I. Since this is the edge of the spectrum where strong instrumental and reduction effects can occur, we will exclude this location from my evaluation, although it would be very interesting for the further discussion of the star. The bump exists in all recorded individual spectra. The spectra were reduced and extracted several times to check

Table 5.2: Line strengths of a set of lines in [AM85] NGC6822 12.

Line	From Level	to Level	Wavelength in Å	line strength in normalized flux
He II	4	3	4686	5.70
He II/H β	8/4	4/2	4868	1.68
He II	7	4	5411	2.04
He II/H α	6/3	4/2	6560	2.95
N V	7	6	4940	1.12
N IV	$1s^2 2s^1 3d^1 \ ^3D_2$	$1s^2 2s^1 3p^1 \ ^3P_1^o$	7110	1.12
C IV	$1s^2 3p^1 \ ^2P_{\frac{1}{2}}^o$	$1s^2 3s^1 \ ^2S_{\frac{1}{2}}$	5801	1.15

this phenomenon. There are no other interesting stellar lines at this location. This was checked with [NIST](#) and with the lines produced in PoWR.

Clumping Clumping plays an important role and contributes to the spectrum. With a clumping factor of 4, which is the default value for WN stars, especially the line shapes on the edges of the lines cannot be reproduced. To obtain such features we need a clumping factor of 10.

Rotational Velocity and co-rotation radius To obtain these broad and especially roundish lines, we need rotational velocities up to 900 km/s. The co-rotation radius does not necessarily need to be increased to improve the spectrum. The wind velocity is around 1200 km/s and changes the width of the lines. The lower the wind speed, the higher the stellar rotation rate. This is assumed to reproduce the observed profile of this kind of emission lines.

5.3 A few words about the other stars

[AM85] NGC6822 3

The triangular but still broad line shapes of that star are similar to that found in other surveys of WR stars (like in [Hamann et al., 2006](#)). Its spectrum is shown in detail in Figure 5.5. The lines are not as roundish as these from [AM85] NGC6822 12 or [AM85] NGC6822 5, and one can also see strong nebula lines. The filenames used for the photometry follow the following structure: hst_11079_10_wfpc2_\$filtername_wf.

Table 5.3: Photometry of [AM85] NGC6822 3 obtained with DAOPhot.

Filter name	f170w	f225w	f336w	f439w ¹	f555w	f814w
Apperent magnitude (mag)	17.72	19.71	18.84	19.23	19.86	20.77
Uncertainty (mag)	0.93	1.42	0.30	-	0.118	0.153
Date (dd.mm.yyyy)	15.11.2009	15.11.2009	15.11.2009	15.11.2009	15.11.2009	15.11.2009

¹ Is only obtained via imexamen task since daofind could not find the star in this image.

Table 5.4: Line strengths of a set of lines in [AM85] NGC6822 3 and the nebula. See Table 2 for further details to spectroscopic language.

Line	From Level	to Level	Wavelength in Å	line strength in normalized flux
N III	$\dots 2s^2 \ ^2P_{1/2}^{\circ}$	$\dots 2s^2 \ ^2D_{3/2}$	4634	1.4
N III	$\dots 2s^2 \ ^2P_{3/2}^{\circ}$	$\dots 2s^2 \ ^2D_{5/2}$	4640	1.75
He II	4	3	4686	3.47
He II/H β	8/4	4/2	4868	1.88
He I	$1s4d \ ^1D_2$	$1s2p \ ^1P_1^{\circ}$	4921	1.61
O III	$\dots 2p^2 \ ^1D_2$	$\dots 2p^2 \ ^3P_1$	4958	1.37
O III	$\dots 2p^2 \ ^1D_2$	$\dots 2p^2 \ ^3P_2$	5006	2.42
He I	$1s2s \ ^1S$	$1s3p \ ^1P_1^{\circ}$	5015	1.24
He II	7	4	5411	1.49
He II/H α	6/3	4/2	6560	5.89
N IV	$\dots 2s3d \ ^3D$	$\dots 2s3p \ ^3P^{\circ}$	7100-7150	1.1-1.3

Table 5.5: Line strengths of a set of lines in [AM85] NGC6822 4 and the nebula.

Line	From Level	to Level	Wavelength in Å	line strength in normalized flux
He II	4	3	4686	1.77
O III	$\dots 2p^2 \ ^1D_2$	$\dots 2p^2 \ ^3P_1$	4958	2.37
O III	$\dots 2p^2 \ ^1D_2$	$\dots 2p^2 \ ^3P_2$	5006	5.21
He II/H β	8/4	4/2	4868	2.16
He II	7	4	5411	1.14
He II/H α	6/3	4/2	6560	1.56/7.60
S II	$\dots 3p^3 \ ^2D_{5/2}$	$\dots 3p^3 \ ^4S_{3/2}$	6716	2.08
S II	$\dots 3p^3 \ ^2D_{3/2}$	$\dots 3p^3 \ ^4S_{3/2}$	6731	1.73

[AM85] NGC6822 4

The prominent Oxygen and Sulfur lines of the nebula are immediately noticeable upon first examination of this spectrum. In contrast, the stellar lines are weaker and in the case of H α and H β a combination of stellar and nebula line. This can be seen in Figure 5.4.

[AM85] NGC6822 5

The spectrum of this star can be seen in spectrum 5.3. Due to the absorption lines inside the brought stellar wind lines, this star is likely to have a companion and the spectrum is composite. To have a first indicator we fitted two Gaussian functions (see equation 5.1) on the observation with the goal to reproduce it.

$$y(x) = a_1 \cdot \exp\left(\frac{-(x-x_1)^2}{2\sigma_1^2}\right) + a_2 \cdot \exp\left(\frac{-(x-x_2)^2}{2\sigma_2^2}\right) + b \quad (5.1)$$

Figure 5.7: Fitting of the emission line at $\lambda 6560 \text{ \AA}$ with two Gaussian functions. The absorption feature at $\lambda 6552 \text{ \AA}$ can be reproduced. From the fitting procedure one can calculate the Doppler shift of the two objects which is given by v_1 and v_2 .

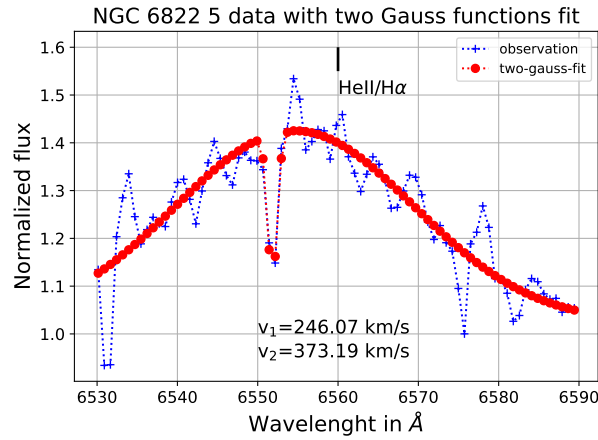


Table 5.7: Line strengths of a set of lines in [AM85] NGC6822 5

Line	From Level	to Level	Wavelength in \AA	line strength in normalized flux
He II	4	3	4686	2.20
O III	$\dots 2p^2 \ ^1D_2$	$\dots 2p^2 \ ^3P_1$	4958	1.30
O III	$\dots 2p^2 \ ^1D_2$	$\dots 2p^2 \ ^3P_2$	5006	2.49
He II/ $H\beta$	8/4	4/2	4868	1.14
He II	7	4	5411	1.29
He II/ $H\alpha$	6/3	4/2	6560	1.41
S II	$\dots 3p^3 \ ^2D_{5/2}$	$\dots 3p^3 \ ^4S_{3/2}$	6716	0.83
S II	$\dots 3p^3 \ ^2D_{3/2}$	$\dots 3p^3 \ ^4S_{3/2}$	6731	0.90

where $a_{1,2}$, b , $\sigma_{1,2}$ are fitting parameter and $x_{1,2}$ are the wavelengths of the corresponding lines. It is only shown in Figure 5.7 for the line at $\lambda 6560 \text{ \AA}$. But this feature can be reproduced at $\lambda 4868 \text{ \AA}$ and $\lambda 5411 \text{ \AA}$ as well.

Table 5.6: Photometry of [AM85] NGC6822 5 obtained with DAOPhot.

Filter name	f225w ¹	f336w	f439w	f555w	f656n ¹
Apperent magnitude (mag)	18.59	19.19	19.56	20.05	15.86
Uncertainty (mag)	-	0.348	0.301	0.129	-
Date (dd.mm.yyyy)	06.11.2009	06.11.2009	06.11.2009	06.11.2009	06.11.2009

¹ is only obtained via imexamen task since daofind could not find the star in this image.

The Photometry of this object was achieved with the following HST structure for the image names: hst_06567_07_wfpc2_\$filtername_wf. You can find and download the HST images on the [MAST archive](#)⁴.

⁴link in Table 1 in the Appendix.

Results

All stars show features which lead to new results. They will help us to understand the nature of WR stars in detail. In Table 6.1, the reader can find a table with all stellar properties obtained from the analysis of the spectrum.

6.1 [AM85] NGC6822 WR12

The previous literature and this study agree, that this star contains no hydrogen (<5%) which is unique in a galaxy with such low metallicity. Furthermore, the most eye-catching phenomenon in its spectrum are the roundish line profiles which was previously observed in WR stars in the MW or LMC (see [Shenar et al., 2014](#)) but never in a low metallicity galaxy like NGC 6822.

After [Shenar et al. \(2014\)](#), the round line profile indicates a high rotation speed of the star as well as a high wind co-rotation radius. This phenomenon has already been studied for stars in the LMC by [Shenar et al. \(2014\)](#). According to their research, the magnetic field that would

Table 6.1: Summary of parameters of the four WR stars.

Properties/Stars	[AM85] NGC6822 3	[AM85] NGC6822 4	[AM85] NGC6822 5	[AM85] NGC6822 12
Right ascension ^a (J2000)	19:44:31.98	19:44:38.00	19:44:49.40	19:45:13.47
Declination ^a (J2000)	-14:44:09.100	-14:51:07.7	-14:45:40.9	-14:45:12.3
Type ^b	WNL	WNL	WNE (WN2)	WNE (WN4/WC4) -b
$E(B - V)$ [mag]	0.38	0.38	0.5	0.29±0.05
Binary?	Single	Single	Binary?	Single
T [kK]	39.8	79.4	125.9	82.5±5
$v_{rad,*}$ [km s ⁻¹]	-50	-50	-50	-50±5
$\log(\dot{M})$ [M _⊙ yr ⁻¹]	-6.1	-6.4	-5.8	-5.0±0.2
M [M _⊙]	33	12	12	31 ⁺¹⁰ ₋₂
M_V [mag]	-4.84	-4.73	-5.21	-5.32±0.3
$\log(L)$ [L _⊙]	5.2 ± 0.5	6.1	6.55	6.15 ^{+0.1} _{-0.3}
R_T [R _⊙]	39.8	19	7.9	6.4±1
R [R _⊙]	9.4	2.4	0.9	4.9±1

^a[Armandroff & Massey \(1985\)](#), ^b following criteria in [van der Hucht \(2001\)](#) Table 2, there are no errors given for Grid models.

explain these properties can be calculated with the following formula:

$$B_*^2 \approx M_A^2 \cdot R_{cor} \cdot B_*^2, \quad (6.1)$$

$$= \frac{\dot{M} v_\infty}{R_*^2} \left(1 - \frac{R_*}{R_{cor}}\right) \cdot \left(\frac{R_{cor}}{R_*}\right)^2, \quad (6.2)$$

where M_A is the Alfvénic Mach number and R_{cor} the co-rotation radius. However, this assumption is valid if we calculate with the beta law $\beta = 1$ and assume that the Mach number at the co-rotation radius corresponds to that at the Alfvén radius. Through the described magnetic field, the angular momentum is transferred from the stellar rotation to the wind. The time until all the angular momentum energy is transferred to the wind is called spin-down time. It can be calculated via:

$$\tau_J = J J^{-1} \approx \frac{3}{5} \frac{M_* R_*^2}{\dot{M} r_A^2}, \quad (6.3)$$

$$\approx \frac{3}{5} \frac{M_* R_*^2}{\dot{M} R_{cor}^2}, \quad (6.4)$$

where we assume here that $r_A = R_{cor}$ (Friend & MacGregor, 1984; Hartmann & MacGregor, 1982). r_A is the Alfvén radius and R_{cor} the co-rotation radius. The rotational velocity must not exceed a critical point, otherwise matter will be released from the stellar surface into its surroundings by rotation. This critical velocity describes the point at which the gravitational force and centrifugal force are equal and can be given by:

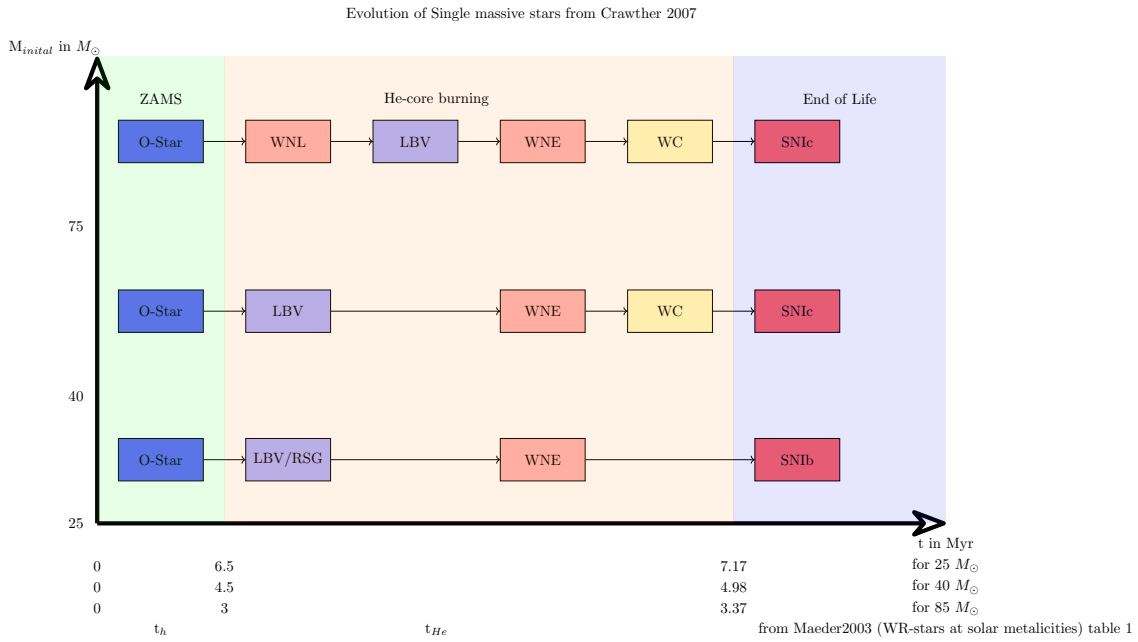
$$v_{crit} = \sqrt{\frac{GM(r)}{r}}, \quad (6.5)$$

where G is the gravitational constant, $M(r)$ is a function of the mass of an object depending on the radius Maeder (2008).

For [AM85] NGC6822 12 it is possible to reconstruct the observation without an increased co-rotation radius. Nevertheless, some lines, like He II $\lambda 4686 \text{ \AA}$ or He II/H α $\lambda 6560 \text{ \AA}$, get a rounder shape with increased co-rotation radius. This implies that these lines originate in the outer layers of the star at 2-3 stellar radii. A corresponding magnetic field of 987.91 G or 1711.12 G respectively, would be needed to satisfy such radii. Taking into account the spindown time, the life time of the WR star would shrink drastically from 1.86 Myr to 0.47 Myr to 0.21 Myr with $R_{cor} = [1, 2, 3]$, respectively. Additionally [AM85] NGC6822 12 rotates with $\sim 82\%$ of its critical rotational velocity. Due to this rotation the star is deformed/stretched to an ellipsoid and not a sphere as usually assumed.

The credibility of the models, the magnetic field and further questions which arise here are discussed in chapter 7. The subset of stars in Shenar et al. (2014) are also of WNE type and lie in the outer region of the LMC where the metallicity is assumed to be lower than in the center

Figure 6.1: Evolution of Life of a WR star at solar metallicity with different masses. This picture was made using the information from Crowther (2007) and Meynet & Maeder (2003). Colors have no significance, they only serve to provide structure to the overview.



of the galaxy.

Since [AM85] NGC6822 12 contains no, or only a few percent of hydrogen, combined with its mass of under $40 M_{\odot}$, it is a highly evolved object. Compared to single stars at solar metallicity it only has a few thousand years left until it presumably explodes in a supernova type Ib (see Figure 6.1).

Classification of WN Stars The classification of main and sub categories for our sample of stars, were made using the criteria from van der Hucht (2001). They are listed in Tables 3,4 and Figure 2.

Discussion

On the theoretical explanation of the round shape of emission lines in [AM85] NGC6822 12

Only considering high wind velocity is not enough to reproduce the observed line shape. The broad and round lines suggest a high rotation rate, close to its critical velocity. It therefore becomes distorted and the spherical symmetric case might not be applicable anymore. This phenomenon could be explained assuming that [AM85] NGC6822 12 is a newly formed merger product. However, hydrogen would be present in such a case, except the companion was a WR star without hydrogen. [Shenar et al. \(2014\)](#) gives many possible explanations for this phenomenon which to this point were not researched further. He mentions that the needed magnetic fields of order kG are not detected until now in WR stars, and thus might not be plausible. It is still not settled how these lines are produced.

The χ^2 -Method The applicability of the χ^2 -Method is disputable because nebula lines and artifacts can lead to an error. A more accurate way is to select an area around the spectral lines, which belong to the star and its wind, and calculate the χ^2 value from this selection. This was done using the `findgrids.py` script which is explained in detail in the appendix (section 8). Although this method was applied it still can only give a direction where to search for a best fitting model. The control by eye and brain needs still to be done.

The best fitting model for the observation of [AM85] NGC6822 12, for instance, has a smaller χ^2 value than every model of the individual calculated ones. But, we calculated the grid model with the same parameter again and achieved another spectrum. The grid model was calculated with an earlier version of PoWR where the iron content was differently handled¹. If one had used models from the website before July 2022 they might be wrong. But since we used the newest PoWR version this problem is not important for the thesis but does not save for other errors which might be detected in the future.

Subtraction and extraction The subtraction and extraction of the science images from the ESO, are discussable because `ESOREFLEX` is not self written and serves as a Black box. As has

¹Detailed Information can be found in `~wrh/PoWR-Memos.dir/20180219.txt`.

been outlined in section 4.3, with some configuration it extracts too much. Especially at the edges of a spectrum the program shows its limits. The wavelength calibration on the other hand provides reasonable results. The self-extracted spectra are equal to the pipeline extracted ones by the experts. Two months after extracting them individually, the ESO provided their extracted spectra from the data.

Metallicity: Although the metallicity can change a lot inside the galaxy, the assumption to use a similar one to the SMC worked out well in the end. Changing the abundances to the ones used in the LMC model grids would result in too strong nitrogen and carbon lines.

Chapter 8

Summary and outlook

In this thesis we have seen the interplay between observation, theory, and modeling. Chapter one and two described an historic overview about the topic. These fascinating objects have the potential to give us insights about philosophic questions like where we come from but also new physical phenomenon like the broad roundish line profiles we have seen in Chapter six.

My work is described in detail in Chapter four to six. It was necessary to learn how to work with new programs like `ESOREFLEX`, `POWR`, `Fortran`, `IRAF`. Furthermore, self written python scripts made the life with different data sources a lot easier and trained my Python skills. The subtraction and extraction of telescope data as well as the communication with the telescope group and preparation of the observations gave insights to the observational side of Astrophysics.

Additionally, working with `POWR`, calculating and fitting a model to the observation let me take a look behind the theoretical side of Astrophysics. All courses which I took in the Astrophysics master degree, are combined in this thesis. From Cosmic Magnetic fields, gravitational waves, stars and stellar evolution, galaxy and cosmology over to spectroscopy, stellar winds and history of Astrophysics. The last chapter described the results and the discussion of the project. All classes which I took helped to understand what to conclude and how to interpret the observational data.

In conclusion, we categorized the WR stars, [AM85] NGC6822 3, [AM85] NGC6822 4, [AM85] NGC6822 5, [AM85] NGC6822 12 to be of type WNL, WNL, WNE, WNE, respectively. Furthermore, we detected possible binary features in [AM85] NGC6822 5 and found that one does not need a high co-rotation value to reproduce the round shape profiles of [AM85] NGC6822 12. The metallicity plays an important role since these round shape profiles only occurred in stars which lie in regions with a lower metallicity compared to the center of a galaxy. The main results can be seen in Table 6.1. We estimated the photometry of all stars new and obtained a spectral catalog of four sources in particular. The spectra of many other sources, are extracted and wait to be analyzed.

Outlook Since one could argue that [AM85] NGC6822 12 might have been a merger product and had strong broadened lines and [AM85] NGC6822 5 shows also very roundish lines with clear binary indications, a future work could look at possible similarities between binarity and a round line profile. This work contained multiple spectra from different sources which still can be analyzed. Especially the H II region analysis would make a great bachelor Thesis to check the metallicity in this region. Furthermore, the analyzation of the three other main objects would make another good topic for a thesis. With the knowledge gained in this work, one should apply for more observation time in the UV as well as a multi-era spectral series. Through the UV observation we would be able to estimate the parameters of all stars a lot better, since we need to fit more lines. The multi-era spectra would make it possible to study changes in the behavior of the wind of [AM85] NGC6822 12. Moreover, with both mentioned observation types it is possible to get more information about the binarity of [AM85] NGC6822 5. The bright X-Ray point source in the center of NGC 6822 makes an interesting observational object, too. One could also take a more detailed look at the mass loss - metallicity relation.

Acronyms and Glossary

- AGB** Asymptotic giant branch. 12
- BH** Black Hole. 1, 8
- CCD** Charge-coupled device. 15–18, 51
- DAOphot** A name for a method to obtain photometric values. 22, 23
- DSS** Digital Sky Survey. 14, 18, 50, 51
- ESO** European Southern Observatory. 1, 11, 18, 42, 50
- ESOREFLEX** Program to reduce spectroscopic data from the VLT. ii, iii, 18, 19, 43
- FORS** FOcal Reducer and low dispersion Spectrograph. 16–18
- FWHM** Full width half maximum. 17
- GRB** Gamma Ray Burst. 8
- HRD** Hertzsprung-Russel Diagram. 2, 25, 26, 51
- HST** Hubble Space Telescope. 15, 19, 22–24, 35, 51
- Image Reduction and Analysis Facility** Powerful analysis-program for astronomical purposes. 18, 24
- LMC** Large Magellanic Cloud. 1, 3, 11, 12, 32, 37, 38, 42, 53
- LSS** long slit spectroscopy. 17
- LTE** Local Thermal Equilibrium. 4
- MW** Milky Way. 1, 3, 37
- NS** Neutron Star. 1, 8
- PoWR** Potsdam Wolf Rayet Modelling Code. ii, iii, 1, 4, 5, 7, 33, 41, 43
- RGB** Red giant branch. 12
- rgb** Red-green-blue. 17
- SAOds9** Program to investigate fits files and arrange them.. 13, 14, 17, 21, 53
- SED** Spectral Energy Distribution. 5, 21, 23, 25, 26, 31, 52
- Sextractor** A name for a method to obtain photometric values. 22
- SMC** Small Magellanic Cloud. ii, iii, 1, 3, 8, 11–13, 25, 26, 42, 50, 51, 53
- SN** Supernova. 1, 7
- SNR** Signal to Noise ratio. 17
- TRGB** Tip of the red giant branch. 12
- UV** Ultra violett. 21, 44
- VLT** Very large Telescope. ii, iii, 1, 16, 18, 20, 51
- WR** Wolf-Rayet. ii, iii, v, 1–4, 7–9, 14–16, 19–21, 25, 26, 33, 37–39, 41, 43, 50–53
- ZP** Zero point. 23, 24

Bibliography

- Appenzeller, I., Fricke, K., Fürtig, W., et al. 1998, *The Messenger*, 94, 1 4.2
- Armandroff, T. E., & Massey, P. 1985, *ApJ*, 291, 685 4.1, 4.2, 4.5, 5.2, 6.1, 8
- Asplund, M., Grevesse, N., Sauval, A. J., & Scott, P. 2009, *Annual Review of Astronomy and Astrophysics*, 47, 481 2.2
- Barnard, E. E. 1884, *Astronomische Nachrichten*, 110, 125 1
- Beals, C. 1940, *Journal of the Royal Astronomical Society of Canada*, 34, 169 2.1
- Bianchi, L., Scuderi, S., Massey, P., & Romaniello, M. 2001, *ApJ*, 121, 2020 4.4, 5.2, 5.2, 5.2, 8
- Castor, J. I., Abbott, D. C., & Klein, R. I. 1975, *ApJ*, 195, 157 2.3
- Cioni, M.-R. 2009, *A&A*, 506, 1137 3.2
- Conti, P. 1976 2.4
- Conti, P. S., Massey, P., & Garmany, C. D. 1989, *ApJ*, 341, 113 2.1
- Crowther, P. A. 2007, *Annual Review of Astronomy and Astrophysics*, 45, 177 2, 2.3, 2.3, 2.4, 2.4, 6.1, 8
- Crowther, P. A., & Hadfield, L. 2006, *A & A*, 449, 711 2.3
- Davis, L. E. 1994 4.4
- De Vaucouleurs, G., De Vaucouleurs, A., Corwin, J., et al. 1991, *Third Reference Catalogue of Bright Galaxies, Version 3.9*. Springer, New York, NY 3
- Eldridge, J. J., & Vink, J. S. 2006, *A&A*, 452, 295 2.4
- Eskridge, P. B., & Raymond E., I. W. 1997, *ApJ*, 114, 988 3
- ESO. 1998, FORS at VLT UT1 Cassegrain focus 4.2, 8
- . 2009, Barnards Galaxy, <https://www.eso.org/public/images/eso0938a/>, accessed: 2023-03-04 3.1, 8
- . 2022, FORS2 User manual, https://www.eso.org/sci/facilities/paranal/instruments/fors/doc/VLT-MAN-ESO-13100-1543_P110.2.pdf, accessed: 2023-03-04 4.2
- . 2023, FORS2, FOcal Reducer/low dispersion Spectrograph 2, <https://www.eso.org/sci/facilities/paranal/instruments/fors/overview.html>, accessed: 2023-03-04 4.2
- Freudling, W., Romaniello, M., Bramich, D. M., et al. 2013, *A&A*, 559, A96 4.3
- Friend, D. B., & MacGregor, K. B. 1984, *ApJ*, Part 1 (ISSN 0004-637X), vol. 282, July 15, 1984, p. 591-602., 282, 591 6.1
- Fusco, F., Buonanno, R., Bono, G., et al. 2012, *A&A*, 548, A129 3.1
- Gräfener, G., Koesterke, L., & Hamann, W. R. 2002, *A&A*, 387, 244 2.2
- Hainich, R., Pasemann, D., Todt, H., et al. 2015, *A&A*, 581, A21 2, 5.1, 8
- Hainich, R., Shenar, T., Sander, A., Hamann, W.-R., & Todt, H. 2016, *Proceedings of the International Astronomical Union*, 12, 171 3
- Hainich, R., Rühling, U., Todt, H., et al. 2014, *A&A*, 565, A27 2
- Hamann, W. R., Graefener, G., & Liermann, A. 2006, *A&A*, 457, 1015 5.3
- Hamann, W. R., & Gräfener, G. 2003, *A&A*, 410, 993 2.2
- Hamann, W.-R., Oskinova, L., Todt, H., et al. 2016, *Proceedings of the International Astronomical Union*, 12, 223–227 2
- Hamann, W.-R., Sander, A., & Hamann, D. M. 2016, POWR, <https://www.astro.physik.uni-potsdam.de/~wrh/PoWR/powrgrid1.php>, accessed: 2023-03-04 5.1
- Hamann, W.-R., & Todt, H. 2023, *ManPoWR - the PoWR code manual*, <https://www.astro.physik.uni-potsdam.de/~htodt/manpowr.pdf>, accessed: 2023-03-04 4.2

- 2023-03-04 2.2, 2.1, 2.2, 2.2, 8
- Hartmann, L., & MacGregor, K. 1982, *ApJ*, Part 1, vol. 259, Aug. 1, 1982, p. 180-192., 259, 180 6.1
- Johnson, H., & Morgan, W. 1951, *ApJ*, 114, 522 4.4
- Kippenhahn, R., Weigert, A., & Weiss, A. 2014, *Stellar Structure and Evolution*, *Astronomy and Astrophysics Library* (Springer Berlin Heidelberg) 2.1
- Kirby, E. N., Cohen, J. G., Guhathakurta, P., et al. 2013, *ApJ*, 779, 102 3.2
- Koornneef, J., Bohlin, R., Buser, R., Horne, K., & Turnshek, D. 1986, *Highlights of Astronomy*, 7, 833 4.4
- Maeder, A. 2008, *Physics, Formation and Evolution of Rotating Stars*, *Astronomy and Astrophysics Library* (Springer Berlin Heidelberg) 6.1
- Maiolino, R., & Mannucci, F. 2019, *A&A Rev.*, 27, 3 3
- Marconi, M., Molinaro, R., Ripepi, V., et al. 2017, *Monthly Notices of the Royal Astronomical Society*, 466, 3206 3.1
- Massey, P., Armandroff, T. E., Pyke, R., Patel, K., & Wilson, C. D. 1995, *ApJ*, 110, 2715 3, 3
- Massey, P., & Davis, L. E. 1992 4.4
- Massey, P., Olsen, K. A. G., Hodge, P. W., et al. 2007, *ApJ*, 133, 2393 4.4
- Meynet, G., & Maeder, A. 2003, *A&A*, 404, 975 6.1, 8
- Musella, I., Marconi, M., Stetson, P., et al. 2016, *Monthly Notices of the Royal Astronomical Society*, 457, 3084 3.1
- Namumba, B., Carignan, C., Passmoor, S., & de Blok, W. J. 2017, *Monthly Notices of the Royal Astronomical Society*, 472, 3761 3
- Oskinova, L. M., Hamann, W.-R., & Feldmeier, A. 2007, *A&A*, 476, 1331 2.2
- Pfund, A. H. 1924, *J. Opt. Soc. Am.*, 9, 193 5.2
- Pilyugin, L. 2001, *A&A*, 374, 412 3.2
- Rich, J. A., Persson, S., Freedman, W. L., et al. 2014, *ApJ*, 794, 107 3, 3.1
- Sander, A., Shenar, T., Hainich, R., et al. 2015, *A&A*, 577, A13 2.2
- Sander, A. A. C., Vink, J. S., & Hamann, W.-R. 2019, *Monthly Notices of the Royal Astronomical Society*, 491, 4406 1
- Sander, A., Hamann, W.-R., & Todt, H. 2012, *A&A*, 540, A144 2
- Schlafly, E. F., & Finkbeiner, D. P. 2011, *ApJ*, 737, 103 3
- Shenar, T. 2022, *Wolf-Rayet stars: recent advances and persisting problems* 2, 2.4, 2.2, 8
- Shenar, T., Hamann, W. R., & Todt, H. 2014, *A&A*, 562, A118 6.1, 6.1, 7
- Shenar, T., Hainich, R., Todt, H., et al. 2016, *A&A*, 591, A22 5.1, 8
- Sibbons, L., Ryan, S. G., Napiwotzki, R., & Thompson, G. 2015, *A&A*, 574, A102 3.2
- Smith, L. F. 1968, *Monthly Notices of the Royal Astronomical Society*, 138, 109 2.1
- Space Telescope Science Institute. 2022, *HST User Documentation*, <https://hst-docs.stsci.edu/acsdhb/chapter-5-acs-data-analysis/5-1-photometry>, accessed: 2023-03-04 4.4, 4.4
- Swinburne University of Technology. 2023, *Interstellar Reddening*, <https://astronomy.swin.edu.au/cosmos/I/Interstellar+Reddening>, accessed: 2023-03-04 4.4
- Taibi, S., Battaglia, G., Leaman, R., et al. 2022, *A&A*, 665, A92 3.2, 3
- Tantalo, M., Dall’Ora, M., Bono, G., et al. 2022, *ApJ*, 933, 197 3.2
- Todt, H., Sander, A., Hainich, R., et al. 2015, *A&A*, 579, A75 3
- Tody, D. 1986, in *Society of Photo-Optical Instrumentation Engineers (SPIE) Conference Series*, Vol. 627, *Instrumentation in astronomy VI*, ed. D. L. Crawford, 733 4.4
- Tody, D. 1993, in *Astronomical Society of the Pacific Conference Series*, Vol. 52, *Astronomical Data Analysis Software and Systems II*, ed. R. J. Hanisch, R. J. V. Brissenden, & J. Barnes, 173 4.4
- Université de Strasbourg/CNRS. 2023, *Hips2Fits*, <https://alasky.u-strasbg.fr/hips-image-services/hips2fits>, accessed: 2023-03-04 3.3, 8
- van der Hucht, K. A. 2001, *New Astronomy Reviews*, 45, 135 2, 2.1, 6.1, 6.1, 8, 8, 3, 4, 2
- Venn, K., Lennon, D., Kaufer, A., et al. 2001, *ApJ*, 547, 765 3.2
- Westerlund, B., Azzopardi, M., Breysacher, J., & Lequeux, J. 1983, *A&A*, 123, 159 5.2

- Wolf, C. J. E., & Rayet, G. 1867, Academie des Sciences Paris Comptes Rendus, 65, 292 2
- Woosley, S., & Bloom, J. 2006, Annu. Rev. Astron. Astrophys., 44, 507 2.4

List of Figures

1.1	Spectra of [AM85] NGC 6822 12 plotted with the visual colors where dark blue is at 3800 Å and dark red is at 7200 Å. This displays the color range of our eye.	2
2.1	Structure of a PoWR model calculation from the PoWR manual (Hamann & Todt, 2023)	5
2.2	Figure 2 from Shenar (2022) , red circles are binaries. Only stars with a minimal luminosity exhibit winds to be classified as a WR star. In the SMC stripped stars need a minimal luminosity of 5.6 mag and a minimal initial mass of $\approx 40 M_{\odot}$ to be viewed as WR star.	8
2.3	Credit: Cmglee, CC BY-SA 3.0 (licence link), via Wikimedia Commons, Data reference: Jennifer Johnson (OSU); Nasa's astronomy picture of the day 09.08.2020 ; The periodic table shows the origin of the elements. The filling of each element represents the percentage by which element contributes to the production of this element. Among them are exploding massive stars and merging neutron stars which have WR stars as progenitors.	9
3.1	An image of Barnard's Galaxy (ESO, 2009). The ESO used the Wide Field Imager attached to the 2.2-metre MPG/ESO telescope at ESO's La Silla Observatory. North is upwards. The image contains B, V, R, and H-alpha filter. Its field of view is 35×34 arcmin.	11
3.2	Schematic explanation of angular distance. We assume a right angular triangle for this problem with the geometrical advantage to use formula 3.5. The black star represents a target stars. The eye represents the observer on earth.	13
3.3	This is an image from NGC 6822 , made via the help of hips2fits (Université de Strasbourg/CNRS, 2023) . It is a combined image, of DSS red and DSS blue, in grey scale. The green circles mark our sample of WR stars. The middle magenta circle marks the center. The length of the magenta arrows indicate the projected distance from the center to the star. These distances are written in Table 3.3.	14
4.1	Filter system to find WR stars as in Armandroff & Massey (1985)	15

4.2	The image shows FORS (yellow), mounted at the Cassegrain focus of the Unit telescope 1 (ESO, 1998).	16
4.3	This is an image from NGC6822, made via the help of hips2fits . It is a combined image, of DSS red and DSS blue, in Grey scale. The green squares mark the CCD field of views + interesting He II regions (Hubble I,II,III,V,X). Our four target stars are marked with green circles. The slit position is marked in yellow. We have spectra from all regions which sit on the yellow slit position. WR+Number+U/L is an abbreviation used during the work progress to name the different CCDs.	18
4.4	The wrong slit position on [AM85] NGC6822 5. Green : acquisition image, red : HST image, Blue : Slit position. Also marked in a red square is the reference star. With the violet lines the position of the WR star is indicated. Because of multiple reasons, acquisition image and HST image object position differ slightly from one another. .	19
4.5	Positions of our sample of WR stars. North is upwards, east is to the left side in every picture. Only [AM85] NGC6822 4 is not an HST image but the acquisition image from the VLT. Each green square has the size of one arc-minute which correspond to length of 137 pc. One can compare it with the Figure 5 in Armandroff & Massey (1985)	20
4.6	The ESOREFLEX starting window for FORS workflow. Under setup directories one needs to change the path to where the data is located. On the bottom one can see a flowchart of the program.	24
5.1	HRD of our sample of stars compared with the sample of WR stars from the SMC from Hainich et al. (2015) and Shenar et al. (2016) . Black errorbars indicate the errors from the literature.	26
5.2	Spectrum of [AM85] NGC6822 12: green boxes indicate Photometry by Bianchi et al. (2001) , blue boxes indicate photometry extracted by IRAF with DAOPHOT. Black shows the observed spectrum, red the model spectrum. Blue is the normalized observed spectrum.	27
5.3	Spectrum of [AM85] NGC6822 5: Black shows the observed spectrum, blue is the normalized Spectrum, red is the model spectrum.	28
5.4	Spectrum of [AM85] NGC6822 4: Black shows the observed spectrum, blue is the normalized Spectrum, red is the model spectrum.	29
5.5	Spectrum of [AM85] NGC6822 5: Black shows the observed spectrum, blue is the normalized Spectrum, red is the model spectrum.	30

5.6	A SED with a Model for [AM85] NGC6822 12 with all possible photometric values. The colors stand for: Sextractor ST-system (yellow color), Sextractor VEGA-system, DAOPHOT ST-system, DAOPHOT VEGA-system, Johnson, IRAF, Bianci with numbers.	31
5.7	Fitting of the emission line at $\lambda 6560 \text{ \AA}$ with two Gaussian functions. The absorption feature at $\lambda 6552 \text{ \AA}$ can be reproduced. From the fitting procedure one can calculate the Doppler shift of the two objects which is given by v_1 and v_2 .	35
6.1	Evolution of Life of a WR star at solar metallicity with different masses. This picture was made using the information from Crowther (2007) and Meynet & Maeder (2003). Colors have no significance, they only serve to provide structure to the overview.	39
1	electron configuration of C: $1s^2 2s^2 2p^2$ looks like:	iii
2	The Table from the seventh catalog of WR stars from van der Hucht (2001). It describes the categorization criteria for WR stars at that time.	iii
3	The observation (dark blue) and the SMC WNE 12-12 model (red) with indications which region of the spectrum contributes to the χ^2 value (light blue boxes)	xiv
4	The χ^2 value evaluated for all SMC model grids. White is the best χ^2 value and black the worst. The best fitting model has a blue square around its position.	xv

List of Tables

3.1	Distance of NGC 6822 from different sources, in comparison with the LMC and SMC.	12
3.2	Metallicity of NGC 6822 from different sources, in comparison with the LMC and SMC	12
3.3	Distance from the center of Barnard's galaxy to the target objects with the calculated iron abundance from equation 3.4. The errors which could occur here are mainly human made and cannot really be estimated. Furthermore, these should be seen as minimal values since in formula 3.4, R is the deprojected radius whereas we could only use a projected radius in SAODs 9.	14
4.1	Used grisms with their spectral resolution (R)	17
5.1	Photometry of [AM85] NGC6822 12 obtained with DA _O phot.	31
5.2	Line strengths of a set of lines in [AM85] NGC6822 12.	33
5.3	Photometry of [AM85] NGC6822 3 obtained with DA _O phot.	33
5.4	Line strengths of a set of lines in [AM85] NGC6822 3 and the nebula. See Table 2 for further details to spectroscopic language.	34
5.5	Line strengths of a set of lines in [AM85] NGC6822 4 and the nebula.	34
5.7	Line strengths of a set of lines in [AM85] NGC6822 5	35
5.6	Photometry of [AM85] NGC6822 5 obtained with DA _O phot.	35
6.1	Summary of parameters of the four WR stars.	37
1	Websites used in the text with the corresponding web address.	i
2	Collection of quantum numbers and formulas.	i
3	Characteristic lines for different WR star types. Taken from van der Hucht (2001) ,	ii
4	Table with additional parameters for characterizing WR Stars, written with information from van der Hucht (2001)	ii
5	Path definitions, where to find what part of my thesis	iv
6	WR12 1200R-1 2022-05-01	v
7	WR12 1200R-2 2022-05-04	v
8	WR12 1440V-1 2022-04-28, WR 12 is in the upper CCD	vi

9	WR12 1440V-2 2022-04-28, WR 12 is in the upper CCD	vi
10	WR4 1200R-1 2022-04-28	vi
11	WR4 1200R-2 2022-05-26	vii
12	WR4 1440V-1 2022-05-28 WR4 is in upper CCD	vii
13	WR4 1440V-2 2022-05-28	vii
14	WR5 1200R-1 2022-05-28	viii
15	WR5 1200R-2 2022-05-31	viii
16	WR5 1440V-1 2022-05-29 Wr 5 is in upper CCD	viii
17	WR5 1440V-2 2022-05-29	ix
18	WR3 1200R-1 2022-05-31 WR3 is in upper CCD	ix
19	WR3 1200R-2 2022-05-31	ix
20	WR3 1440V-1 2022-07-02	x
21	WR3 1440V-2 2022-07-01	x
22	WR5 1200R-1 2022-08-22 is in upper CCD	x
23	WR5 1200R-2 24.08.2022	xi
24	WR5 1440V-1 24.08.2022	xi
25	WR5 1440V-2 24.08.2022	xi
26	Paths to Stars. Usually reduced data is saved under reflexdata/reflexendproducts/. If I didn't add something in particular to the notes I used default parameters in the pipeline. sg+c stands for sky global subtraction + cosmic subtraction. U stands for upper CCD in which usually the target star is contained. L stands for lower CCD. sm stands for sky median subtraction	xii
27	Paths to Stars. Usually reduced data is under reflexdata/reflexendproducts/. I will begin with subfolders of these folders for the stellar spectra. If I didn't add something in particular to the notes I used default parameters in the pipeline. sg+c stands for sky global subtraction + cosmic subtraction. U stands for upper CCD in which usually the target star is contained. L stands for lower CCD. sm stands for sky median subtraction	xiii

Appendix

[AM85] NGC6822 3, [AM85] NGC6822 4, [AM85] NGC6822 5, [AM85] NGC6822 12 are written as WR3, WR4, WR5 and WR12 during the work with the stars since these names are shorter but one must take care to not mix them up with stars which have this name in reality.

Reference links

Table 1: Websites used in the text with the corresponding web address.

Name	reference
Figure 3.1	https://www.eso.org/public/images/eso0938a/
Figure 4.2	https://www.eso.org/public/images/eso9857b/
FORS2 webpage	https://www.eso.org/sci/facilities/paranal/instruments/fors/overview.html
FORS2 user manual	https://www.eso.org/sci/facilities/paranal/instruments/fors/doc/VLT-MAN-ESO-13100-1543_P110.2.pdf
FORS2 Pipeline	https://www.eso.org/sci/software/pipelines/index.html
FORS2 ESOREFLEX toolkit	https://www.eso.org/sci/software/pipelines/index.html#reflex_workflows
PoWR web page	https://www.astro.physik.uni-potsdam.de/~wrh/PoWR/powrgrid1.php
Hips 2 Fits webpage	https://alasky.u-strasbg.fr/hips-image-services/hips2fits
HST user documentation	https://hst-docs.stsci.edu/acsdhb/chapter-5-acs-data-analysis/5-1-photometry
NIST database	https://physics.nist.gov/PhysRefData/ASD/lines_form.html
MAST archive	https://mast.stsci.edu/portal/Mashup/Clients/Mast/Portal.html
SIMBAD database	https://simbad.cds.unistra.fr/simbad/

Helpful definitions

Spectroscopic Language to write population levels:

$$^{2S+1}L_J^{(o)}$$

Quantum number	Formulae	Meaning
n	≥ 1	number of shell
l	$[0, \dots, n-1]$	angular momentum
m	$[-l, \dots, l]$	magnetic projection of l
s	$s = \frac{1}{2}$	Spin
L	$L = \sum l$	composite angular momentum
S	$S = \sum s$	composite spin
J	$J = \sum L + S$	total angular momentum
(o)	$(-1)^{\sum l}$	parity

Table 2: Collection of quantum numbers and formulas.

WN Stars	λ in Å	WC Stars	λ in Å	WO Stars	λ in Å
He I	3888	CII	4267	C IV	5801-5812
He I	4027	CIII	5696	O IV	3400
He I	4471	CIII	4650	O V	5572-5598
He I	5875	CIV	5801-5812	O VI	3811-3834
He II	4200	OV	5572-5598	O VII	5670
He II	4340			O VIII	6068
He II	4541				
He II	4686				
He II	4861				
He II	5411				
He II	6560				
N II	3995				
N III	4634-464				
N III	5314				
N IV	3479-3484				
N IV	4058				
N V	4603				
N V	4619				
N V	4933-4944				

Table 3: Characteristic lines for different WR star types. Taken from [van der Hucht \(2001\)](#),

Additional	Meaning
-A	Hiltner Schild narrow-weak lines and strong continuum
-B	Hiltner Schild broad-strong emission
-w	Hamann for WNE which are early type WN stars, $W_\alpha(\text{HeII}\lambda 5412) > 37\text{\AA}$
-s	Hamann for WNE, $W_\alpha(\text{HeII}\lambda 5412) < 37\text{\AA}$
-b	when $\text{FWHM}(\text{HeII}\lambda 5411) > 30\text{\AA}$ and/or $W_\alpha(\text{HeII}\lambda 5411) > 40\text{\AA}$
-not b	tinier than b
ocillating Balmer Pickering decremet	when $\text{H} + \text{HeII}(\lambda 4861 / \text{HeII}(\sqrt{\lambda 4541 \cdot \lambda 5411})) - 1$ and or $\text{H} + \text{HeII}(\lambda 4340 / \text{HeII}(\sqrt{\lambda 4200 \cdot \lambda 4541})) - 1$
-o	above=0
-(h)	above<0.5
-h	above \geq 0.5
+OB	H absorption without evidence of H-emission
(+OB)	in case of a visual companion
+abs	if absorption lines are of unknown origin
-ha	absorption lines are from WR star with H emission lines.

Table 4: Table with additional parameters for characterizing WR Stars, written with information from [van der Hucht \(2001\)](#).

Figure 1: electron configuration of C: $1s^2 2s^2 2p^2$ looks like:

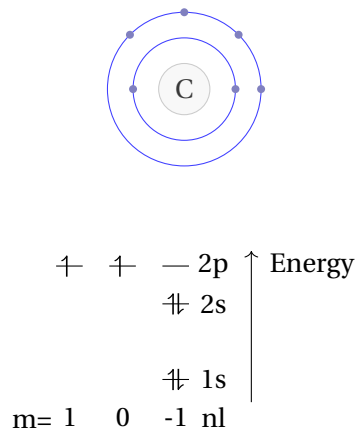


Figure 2: The Table from the seventh catalog of WR stars from [van der Hucht \(2001\)](#). It describes the categorization criteria for WR stars at that time.

Table 2
Smith's (1968a) Wolf-Rayet classification scheme, amended by van der Hucht et al. (1981), Barlow and Hummer (1982), Kingsburgh et al. (1995), Crowther et al. (1995a), and Crowther et al. (1998)^a

WN types	Nitrogen emission lines	Other emission criteria
WN2	N v weak or absent	He II strong
WN2.5	N v present, N IV absent	
WN3	N IV \ll N v, N III weak or absent	
WN4	N IV \approx N v, N III weak or absent	
WN4.5	N IV $>$ N v, N III weak or absent	
WN5	N III \approx N IV \approx N v	
WN6	N III \approx N IV, N v present but weak	He I weak P-Cyg
WN7	N III $>$ N IV, N III $<$ He II 4686	He I strong P-Cyg
WN8	N III \gg N IV, N III \approx He II 4686	He I P-Cyg
WN9	N III $>$ N II, N IV absent	Balmer lines, He I P-Cyg
WN10	N III \approx N II	Balmer lines, He I P-Cyg
WN11	N II \approx He II, N III weak or absent	
WC types	Carbon emission lines	Other emission criteria
WC4	C IV strong, C II weak or absent	O v moderate
WC5	C III \ll C IV	C III $<$ O v
WC6	C III \ll C IV	C III $>$ O v
WC7	C III $<$ C IV	C III \gg O v
WC8	C III $>$ C IV	C II absent, O v weak or absent
WC9	C III $>$ C IV	C II present, O v weak or absent
WO types	Oxygen emission lines	Other emission criteria
WO1	O VII \geq O v, O VIII present	C III absent
WO2	O VII $<$ O v	C IV $<$ O VI, C III absent
WO3	O VII weak or absent	C IV \approx O VI, C III absent
WO4		C IV \gg O VI, C III absent

^a The emission lines used for classifying WN stars are: He I λ 3888, He I λ 4027, He I λ 4471, He I λ 4921, He I λ 5875, He II λ 4200, He II λ 4340, He II λ 4541, He II λ 4686, He II λ 4861, He II λ 5411, He II λ 6560, N II λ 3995, N III λ 4634–4641, N III λ 5314, N IV λ 43479–3484, N IV λ 4058, N v λ 4603, N v λ 4619, and N v λ 4933–4944. The emission lines used for classifying WC stars are: C II λ 4267, C III λ 5696, C III/C IV λ 4650, C IV λ 5801–12, and O v λ 5572–98. The emission lines used for classifying WO stars are: C IV λ 5801–12, O IV λ 3400, O v λ 5572–98, O VI λ 3811–34, O VII λ 5670, and O VIII λ 6068.

Path	Description
~/jstaehle/mydata/ ~/jstaehle/reflex_data/reflex_end_products/ ~/jstaehle/reflex_data/reflex_tmp_prodcuts/ ~/jstaehle/reflex_data/reflex_book_keeping/ ~/jstaehle/reflex_data/reflex_logs/ ~/jstaehle/Masterthesis/ownpythonscripts/ ~/jstaehle/ds9regionfiles/ ~/jstaehle/history.txt ~/jstaehle/finalproducts/	Raw data and Calibration data Pipeline products temporary pipeline prodcuts controlling pipeline prodcuts logs of pipeline procedures My python scripts ds9 region files Helpful commands Final spectra
~/jstaehle/finalproducts/interestingobjects/	further objects with interesting spectra

Table 5: Path definitions, where to find what part of my thesis

Data structure

You can find the Data under <https://www.astro.physik.uni-potsdam.de/~jstaehle/> and is structured in the following way:

What might be unclear is the CHIP column. Since we have one upper and one lower CCD chip it is important to know which is contained in an image. U stands for the upper CCD and L for the Lower CCD. Sometimes the file name selection it is not as straightforward as one might think. For some datasets Upper and Lower CCD are shifted which is marked with an "!".

WR12 1200R-1 2022-05-01

Observed from 07:33:39 to 08:35:24.

Dataset ID/File name	CHIP	Category	Type	Mode
FORS2.2022-05-01T07:37:20.213	1/U	ACQUISITION	SKY	IMAGE
FORS2.2022-05-01T07:37:20.214	2/L	ACQUISITION	SKY	IMAGE
FORS2.2022-05-01T07:43:02.964	1	ACQUISITION	SKY	IMAGE
FORS2.2022-05-01T07:43:02.965	2	ACQUISITION	SKY	IMAGE
FORS2.2022-05-01T07:44:34.621	1	ACQUISITION	SLIT	IMAGE
FORS2.2022-05-01T07:44:34.622	2	ACQUISITION	SLIT	IMAGE
FORS2.2022-05-01T07:45:42.199	1	ACQUISITION	SLIT	IMAGE
FORS2.2022-05-01T07:45:42.200	2	ACQUISITION	SLIT	IMAGE
FORS2.2022-05-01T07:46:39.812	1	ACQUISITION	SLIT	IMAGE
FORS2.2022-05-01T07:46:39.813	2	ACQUISITION	SLIT	IMAGE
FORS2.2022-05-01T07:48:11.489	1	Science	SKY	Spectrum
FORS2.2022-05-01T07:48:11.490	2	Science	SKY	Spectrum

Table 6: WR12 1200R-1 2022-05-01

WR12 1200R-2 2022-05-04

Observed from 07:23:39 to 08:21:11.

Dataset ID/File name	CHIP	Category	Type	Mode
FORS2.2022-05-04T07:26:51.553	1/L	ACQUISITION	SKY	IMAGE
FORS2.2022-05-04T07:26:51.554	2/U	ACQUISITION	SKY	IMAGE
FORS2.2022-05-04T07:29:06.178	1	ACQUISITION	SKY	IMAGE
FORS2.2022-05-04T07:29:06.179	2	ACQUISITION	SKY	IMAGE
FORS2.2022-05-04T07:31:03.886	1	ACQUISITION	SLIT	IMAGE
FORS2.2022-05-04T07:31:03.887	2	ACQUISITION	SLIT	IMAGE
FORS2.2022-05-04T07:32:14.765	1/U!	ACQUISITION	SLIT	IMAGE
FORS2.2022-05-04T07:32:14.766	2/L!	ACQUISITION	SLIT	IMAGE
FORS2.2022-05-04T07:33:58.077	1	Science	SKY	Spectrum
FORS2.2022-05-04T07:33:58.078	2	Science	SKY	Spectrum

Table 7: WR12 1200R-2 2022-05-04

WR12 1440V-1 2022-04-28

Observed from 07:13:19 to 08:11:57.

Dataset ID/File name	CHIP	Category	Type	Mode
FORS2.2022-04-28T07:16:35.465	1/U	ACQUISITION	SKY	IMAGE
FORS2.2022-04-28T07:16:35.466	2/L	ACQUISITION	SKY	IMAGE
FORS2.2022-04-28T07:20:06.551	1	ACQUISITION	SKY	IMAGE
FORS2.2022-04-28T07:20:06.552	2	ACQUISITION	SKY	IMAGE
FORS2.2022-04-28T07:22:16.284	1/L!	ACQUISITION	SLIT	IMAGE
FORS2.2022-04-28T07:22:16.285	2/U!	ACQUISITION	SLIT	IMAGE
FORS2.2022-04-28T07:24:44.044	1	Science	SKY	Spectrum
FORS2.2022-04-28T07:24:44.045	2	Science	SKY	Spectrum

Table 8: WR12 1440V-1 2022-04-28, WR 12 is in the upper CCD

WR12 1440V-2 2022-04-28

Observed from 05:45:13 to 06:46:49.

Dataset ID/File name	CHIP	Category	Type	Mode
FORS2.2022-04-28T05:49:50.974	1/U	ACQUISITION	SKY	IMAGE
FORS2.2022-04-28T05:49:50.975	2/L	ACQUISITION	SKY	IMAGE
FORS2.2022-04-28T05:54:37.181	1	ACQUISITION	SKY	IMAGE
FORS2.2022-04-28T05:49:37.182	2	ACQUISITION	SKY	IMAGE
FORS2.2022-04-28T05:58:12.918	1	ACQUISITION	SLIT	IMAGE
FORS2.2022-04-28T05:58:12.919	2	ACQUISITION	SLIT	IMAGE
FORS2.2022-04-28T05:59:36.533	1/L!	Science	SKY	Spectrum
FORS2.2022-04-28T05:59:36.534	2/U!	Science	SKY	Spectrum

Table 9: WR12 1440V-2 2022-04-28, WR 12 is in the upper CCD

WR4 1200R-1 2022-04-28

Observed from 08:12:07 to 09:07:33.

Dataset ID/File name	CHIP	Category	Type	Mode
FORS2.2022-04-28T08:15:00.925	1/L	ACQUISITION	SKY	IMAGE
FORS2.2022-04-28T08:15:00.926	2/U	ACQUISITION	SKY	IMAGE
FORS2.2022-04-28T08:17:06.956	1	ACQUISITION	SKY	IMAGE
FORS2.2022-04-28T08:17:06.957	2	ACQUISITION	SKY	IMAGE
FORS2.2022-04-28T08:18:34.762	1	ACQUISITION	SLIT	IMAGE
FORS2.2022-04-28T08:18:34.763	2	ACQUISITION	SLIT	IMAGE
FORS2.2022-04-28T08:20:19.725	1/U!	Science	SKY	Spectrum
FORS2.2022-04-28T08:20:19.726	2/L!	Science	SKY	Spectrum

Table 10: WR4 1200R-1 2022-04-28

WR4 1200R-2 2022-05-26

Observed from 08:08:09 to 09:05:09.

Dataset ID/File name	CHIP	Category	Type	Mode
FORS2.2022-05-26T08:12:45.358	1/L	ACQUISITION	SKY	IMAGE
FORS2.2022-05-26T08:12:45.359	2/U	ACQUISITION	SKY	IMAGE
FORS2.2022-05-26T08:14:39.414	1	ACQUISITION	SLIT	IMAGE
FORS2.2022-05-26T08:14:39.415	2	ACQUISITION	SLIT	IMAGE
FORS2.2022-05-26T08:17:55.954	1	Science	SKY	Spectrum
FORS2.2022-05-26T08:17:55.955	2	Science	SKY	Spectrum

Table 11: WR4 1200R-2 2022-05-26

WR4 1440V-1 2022-05-28

Observed from 06:17:12 to 07:17:33.

Dataset ID/File name	CHIP	Category	Type	Mode
FORS2.2022-05-28T06:20:30.122	1/U	ACQUISITION	SKY	IMAGE
FORS2.2022-05-28T06:20:30.123	2/L	ACQUISITION	SKY	IMAGE
FORS2.2022-05-28T06:23:27.504	1	ACQUISITION	SKY	IMAGE
FORS2.2022-05-28T06:23:27.505	2	ACQUISITION	SKY	IMAGE
FORS2.2022-05-28T06:25:29.963	1	ACQUISITION	SKY	IMAGE
FORS2.2022-05-28T06:25:29.964	2	ACQUISITION	SKY	IMAGE
FORS2.2022-05-28T06:27:01.110	1/L!	ACQUISITION	SLIT	IMAGE
FORS2.2022-05-28T06:27:01.111	2/U!	ACQUISITION	SLIT	IMAGE
FORS2.2022-05-28T06:30:20.281	1/L!	Science	SKY	Spectrum
FORS2.2022-05-28T06:30:20.282	2/U!	Science	SKY	Spectrum

Table 12: WR4 1440V-1 2022-05-28 WR4 is in upper CCD

WR4 1440V-2 2022-05-28

Observed from 05:15:38 to 06:16:55.

Dataset ID/File name	CHIP	Category	Type	Mode
FORS2.2022-05-28T05:19:41.991	1/L	ACQUISITION	SKY	IMAGE
FORS2.2022-05-28T05:19:41.992	2/U	ACQUISITION	SKY	IMAGE
FORS2.2022-05-28T05:26:00.364	1	ACQUISITION	SKY	IMAGE
FORS2.2022-05-28T05:26:00.365	2	ACQUISITION	SKY	IMAGE
FORS2.2022-05-28T05:27:44.646	1/U!	ACQUISITION	SLIT	IMAGE
FORS2.2022-05-28T05:27:44.647	2/L!	ACQUISITION	SLIT	IMAGE
FORS2.2022-05-28T05:29:42.114	1	Science	SKY	Spectrum
FORS2.2022-05-28T05:29:42.115	2	Science	SKY	Spectrum

Table 13: WR4 1440V-2 2022-05-28

WR5 1200R-1 2022-05-28 Attention not our star!

Observed from 07:17:47 to 08:25:05.

Dataset ID/File name	CHIP	Category	Type	Mode
FORS2.2022-05-28T07:20:50.311	1/U	ACQUISITION	SKY	IMAGE
FORS2.2022-05-28T07:20:50.312	2/L	ACQUISITION	SKY	IMAGE
FORS2.2022-05-28T07:32:33.276	1	ACQUISITION	SKY	IMAGE
FORS2.2022-05-28T07:32:33.277	2	ACQUISITION	SKY	IMAGE
FORS2.2022-05-28T07:35:37.531	1/L!	ACQUISITION	SLIT	IMAGE
FORS2.2022-05-28T07:35:37.532	2/U!	ACQUISITION	SLIT	IMAGE
FORS2.2022-05-28T07:37:52.416	1	Science	SKY	Spectrum
FORS2.2022-05-28T07:37:52.417	2	Science	SKY	Spectrum

Table 14: WR5 1200R-1 2022-05-28

WR5 1200R-2 2022-05-31 Attention not our star!

Observed from 05:28:14 to 06:29:41.

Dataset ID/File name	CHIP	Category	Type	Mode
FORS2.2022-05-31T05:32:54.215	1/U	ACQUISITION	SKY	IMAGE
FORS2.2022-05-31T05:32:54.216	2/L	ACQUISITION	SKY	IMAGE
FORS2.2022-05-31T05:38:26.760	1	ACQUISITION	SKY	IMAGE
FORS2.2022-05-31T05:38:26.761	2	ACQUISITION	SKY	IMAGE
FORS2.2022-05-31T05:40:18.315	1/L!	ACQUISITION	SLIT	IMAGE
FORS2.2022-05-31T05:40:18.316	2/U!	ACQUISITION	SLIT	IMAGE
FORS2.2022-05-31T05:42:28.017	1	Science	SKY	Spectrum
FORS2.2022-05-31T05:42:28.018	2	Science	SKY	Spectrum

Table 15: WR5 1200R-2 2022-05-31

WR5 1440V-1 2022-05-29 Attention not our star!

Observed from 04:43:31 to 05:44:29.

Dataset ID/File name	CHIP	Category	Type	Mode
FORS2.2022-05-29T04:47:30.829	1/L	ACQUISITION	SKY	IMAGE
FORS2.2022-05-29T04:47:30.830	2/U	ACQUISITION	SKY	IMAGE
FORS2.2022-05-29T04:52:18.305	1	ACQUISITION	SKY	IMAGE
FORS2.2022-05-29T04:52:18.306	2	ACQUISITION	SKY	IMAGE
FORS2.2022-05-29T04:53:25.433	1	ACQUISITION	SKY	IMAGE
FORS2.2022-05-29T04:53:25.434	2	ACQUISITION	SKY	IMAGE
FORS2.2022-05-29T04:55:31.684	1	ACQUISITION	SLIT	IMAGE
FORS2.2022-05-29T04:55:31.685	2	ACQUISITION	SLIT	IMAGE
FORS2.2022-05-29T04:57:16.416	1	Science	SKY	Spectrum
FORS2.2022-05-29T04:57:16.417	2	Science	SKY	Spectrum

Table 16: WR5 1440V-1 2022-05-29 Wr 5 is in upper CCD

WR5 1440V-2 2022-05-29 Attention not our star

Observed from 06:11:27 to 07:06:16.

Dataset ID/File name	CHIP	Category	Type	Mode
FORS2.2022-05-29T06:12:15.557	1/L	ACQUISITION	SKY	IMAGE
FORS2.2022-05-29T06:12:15.558	2/U	ACQUISITION	SKY	IMAGE
FORS2.2022-05-29T06:13:31.607	1	ACQUISITION	SKY	IMAGE
FORS2.2022-05-29T06:13:31.608	2	ACQUISITION	SKY	IMAGE
FORS2.2022-05-29T06:16:52.168	1	ACQUISITION	SLIT	IMAGE
FORS2.2022-05-29T06:16:52.169	2	ACQUISITION	SLIT	IMAGE
FORS2.2022-05-29T06:19:02.571	1	Science	SKY	Spectrum
FORS2.2022-05-29T06:19:02.572	2	Science	SKY	Spectrum

Table 17: WR5 1440V-2 2022-05-29

WR3 1200R-1 2022-05-31

Observed from 07:26:17 to 08:22:32.

Dataset ID/File name	CHIP	Category	Type	Mode
FORS2.2022-05-31T07:29:37.108	1/L	ACQUISITION	SKY	IMAGE
FORS2.2022-05-31T07:29:37.109	2/U	ACQUISITION	SKY	IMAGE
FORS2.2022-05-31T07:31:16.738	1	ACQUISITION	SKY	IMAGE
FORS2.2022-05-31T07:31:16.739	2	ACQUISITION	SKY	IMAGE
FORS2.2022-05-31T07:32:57.229	1	ACQUISITION	SLIT	IMAGE
FORS2.2022-05-31T07:32:57.230	2	ACQUISITION	SLIT	IMAGE
FORS2.2022-05-31T07:35:20.166	1	Science	SKY	Spectrum
FORS2.2022-05-31T07:35:20.167	2	Science	SKY	Spectrum

Table 18: WR3 1200R-1 2022-05-31 WR3 is in upper CCD

WR3 1200R-2 2022-05-31

Observed from 06:29:49 to 07:26:05.

Dataset ID/File name	CHIP	Category	Type	Mode
FORS2.2022-05-31T06:32:19.397	1/U	ACQUISITION	SKY	IMAGE
FORS2.2022-05-31T06:32:19.398	2/L	ACQUISITION	SKY	IMAGE
FORS2.2022-05-31T06:34:35.393	1	ACQUISITION	SKY	IMAGE
FORS2.2022-05-31T06:34:35.394	2	ACQUISITION	SKY	IMAGE
FORS2.2022-05-31T06:36:33.360	1	ACQUISITION	SLIT	IMAGE
FORS2.2022-05-31T06:36:33.361	2	ACQUISITION	SLIT	IMAGE
FORS2.2022-05-31T06:38:52.676	1	Science	SKY	Spectrum
FORS2.2022-05-31T06:38:52.677	2	Science	SKY	Spectrum

Table 19: WR3 1200R-2 2022-05-31

WR3 1440V-1 2022-07-02

Observed from 03:03:27 to 04:01:11.

Dataset ID/File name	CHIP	Category	Type	Mode
FORS2.2022-07-02T03:08:44.070	1/U	ACQUISITION	SKY	IMAGE
FORS2.2022-07-02T03:08:44.071	2/L	ACQUISITION	SKY	IMAGE
FORS2.2022-07-02T03:10:44.269	1	ACQUISITION	SKY	IMAGE
FORS2.2022-07-02T03:10:44.270	2	ACQUISITION	SKY	IMAGE
FORS2.2022-07-02T03:12:12.566	1/L!	ACQUISITION	SLIT	IMAGE
FORS2.2022-07-02T03:12:12.567	2/U!	ACQUISITION	SLIT	IMAGE
FORS2.2022-07-02T03:13:58.819	1	Science	SKY	Spectrum
FORS2.2022-07-02T03:13:58.820	2	Science	SKY	Spectrum

Table 20: WR3 1440V-1 2022-07-02

WR3 1440V-2 2022-07-01

Observed from 04:19:02 to 05:15:37.

Dataset ID/File name	CHIP	Category	Type	Mode
FORS2.2022-07-01T04:22:22.993	1/L	ACQUISITION	SKY	IMAGE
FORS2.2022-07-01T04:22:22.994	2/U	ACQUISITION	SKY	IMAGE
FORS2.2022-07-01T04:24:18.210	1	ACQUISITION	SKY	IMAGE
FORS2.2022-07-01T04:24:18.211	2	ACQUISITION	SKY	IMAGE
FORS2.2022-07-01T04:26:28.393	1/U!	ACQUISITION	SLIT	IMAGE
FORS2.2022-07-01T04:26:28.394	2/L!	ACQUISITION	SLIT	IMAGE
FORS2.2022-07-01T04:28:24.721	1/U!	Science	SKY	Spectrum
FORS2.2022-07-01T04:28:24.722	2/L!	Science	SKY	Spectrum

Table 21: WR3 1440V-2 2022-07-01

WR5 1200R-1 22.08.2022

Observed from 04:21:21 to 05:17:58.

Dataset ID/File name	CHIP	Category	Type	Mode
FORS2.2022-08-22T04:25:05.758	1/U	ACQUISITION	SKY	IMAGE
FORS2.2022-08-22T04:25:05.759	2/L	ACQUISITION	SKY	IMAGE
FORS2.2022-08-22T04:27:15.920	1	ACQUISITION	SKY	IMAGE
FORS2.2022-08-22T04:27:15.921	2	ACQUISITION	SKY	IMAGE
FORS2.2022-08-22T04:28:45.356	1/L!	ACQUISITION	SLIT	IMAGE
FORS2.2022-08-22T04:28:45.357	2/U!	ACQUISITION	SLIT	IMAGE
FORS2.2022-08-22T04:30:44.254	1	Science	SKY	Spectrum
FORS2.2022-08-22T04:30:44.255	2	Science	SKY	Spectrum

Table 22: WR5 1200R-1 2022-08-22 is in upper CCD

WR5 1200R-2 24.08.2022

Observed from 03:09:10 to 04:05:41.

Dataset ID/File name	CHIP	Category	Type	Mode
FORS2.2022-08-24T03:13:52.714	1/U	ACQUISITION	SKY	IMAGE
FORS2.2022-08-24T03:13:52.715	2/L	ACQUISITION	SKY	IMAGE
FORS2.2022-08-24T03:14:58.800	1	ACQUISITION	SKY	IMAGE
FORS2.2022-08-24T03:14:58.801	2	ACQUISITION	SKY	IMAGE
FORS2.2022-08-24T03:16:32.949	1/L!	ACQUISITION	SLIT	IMAGE
FORS2.2022-08-24T03:16:32.950	2/U!	ACQUISITION	SLIT	IMAGE
FORS2.2022-08-24T03:18:27.665	1	Science	SKY	Spectrum
FORS2.2022-08-24T03:18:27.666	2	Science	SKY	Spectrum

Table 23: WR5 1200R-2 24.08.2022

WR5 1440V-1 24.08.2022

Observed from 00:48:34 to 01:44:19.

Dataset ID/File name	CHIP	Category	Type	Mode
FORS2.2022-08-24T00:52:15.895	1/L	ACQUISITION	SKY	IMAGE
FORS2.2022-08-24T00:52:15.896	2/U	ACQUISITION	SKY	IMAGE
FORS2.2022-08-24T00:53:39.128	1	ACQUISITION	SKY	IMAGE
FORS2.2022-08-24T00:53:39.129	2	ACQUISITION	SKY	IMAGE
FORS2.2022-08-24T00:55:15.938	1	ACQUISITION	SLIT	IMAGE
FORS2.2022-08-24T00:55:15.939	2	ACQUISITION	SLIT	IMAGE
FORS2.2022-08-24T00:57:06.082	1	Science	SKY	Spectrum
FORS2.2022-08-24T00:57:06.083	2	Science	SKY	Spectrum

Table 24: WR5 1440V-1 24.08.2022

WR5 1440V-2 24.08.2022

Observed from 01:44:33 to 02:39:51.

Dataset ID/File name	CHIP	Category	Type	Mode
FORS2.2022-08-24T01:48:18.090	1/L	ACQUISITION	SKY	IMAGE
FORS2.2022-08-24T01:48:18.091	2/U	ACQUISITION	SKY	IMAGE
FORS2.2022-08-24T01:49:25.736	1	ACQUISITION	SKY	IMAGE
FORS2.2022-08-24T01:49:25.737	2	ACQUISITION	SKY	IMAGE
FORS2.2022-08-24T01:50:58.344	1	ACQUISITION	SLIT	IMAGE
FORS2.2022-08-24T01:50:58.345	2	ACQUISITION	SLIT	IMAGE
FORS2.2022-08-24T01:52:38.125	1	Science	SKY	Spectrum
FORS2.2022-08-24T01:52:38.126	2	Science	SKY	Spectrum

Table 25: WR5 1440V-2 24.08.2022

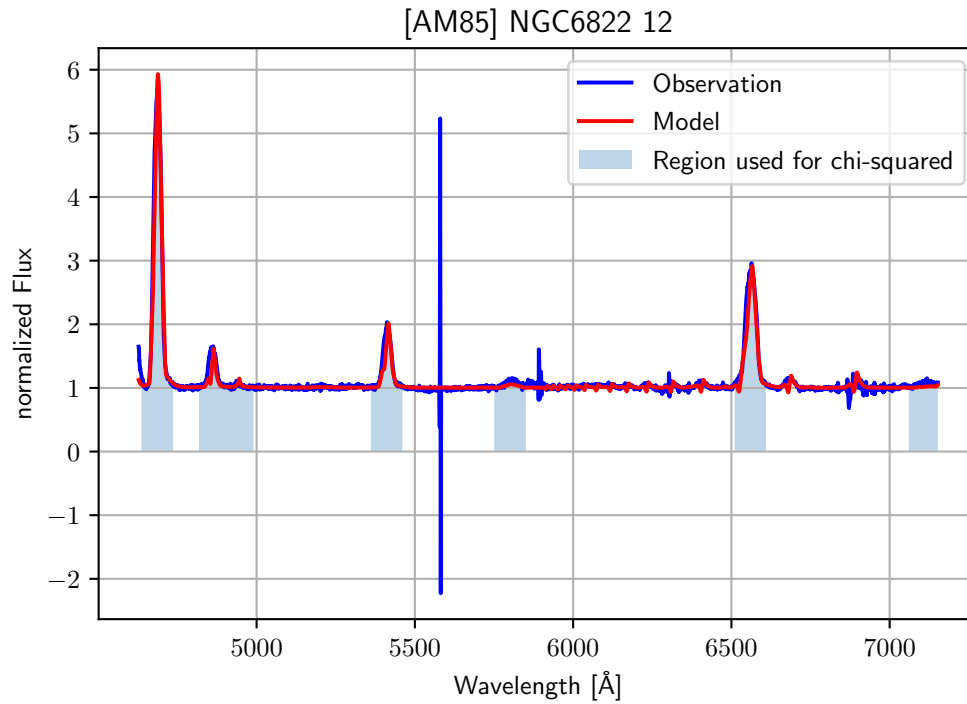
Path	Star	Parameter reduction	Notes	No. of spectrumfile
/2022-07-18T09:20:34/FORS2.2022-05-01T07:48:11.4897/	WR12 1200R-1 2022-05-01 U	sg+c	- -	6
/2022-07-18T09:20:34/FORS2.2022-05-01T07:48:11.490/	WR12 1200R-1 2022-05-01 L	sg+c	- -	-
/2022-07-18T09:20:34/FORS2.2022-05-04T07:33:58.078/	WR12 1200R-2 2022-05-04 U	sg+c	- -	5
/2022-07-18T09:20:34/FORS2.2022-05-04T07:33:58.077/	WR12 1200R-2 2022-05-04 L	sg+c	- -	-
/2022-07-08T15:14:09/FORS2.2022-04-28T07:24:44.044/	WR12 1440V-1 2022-04-28 U	sg+c	no sky/ISM/Cosmic lines/points	9
/2022-07-18T09:20:34/FORS2.2022-04-28T07:24:44.045/	WR12 1440V-1 2022-04-28 L	sg+c	- -	-
/2022-07-08T15:14:09/FORS2.2022-04-28T05:59:36.534/	WR12 1440V-2 2022-04-28 U	sg+c	- -	6
/2022-07-18T09:20:34/FORS2.2022-04-28T05:59:36.533/	WR12 1440V-2 2022-04-28 L	sg+c wdeg=4 pd=80	bc residuals<0.5	-
/2022-07-20T13:54:52/FORS2.2022-04-28T08:20:19.7257/	WR4 1200R-1 2022-04-28 U	sm	- -	7
/2022-07-20T13:54:52/FORS2.2022-04-28T08:20:19.726/	WR4 1200R-1 2022-04-28 L	sg+c	- -	-
/2022-07-20T13:54:52/FORS2.2022-05-26T08:17:55.955/	WR4 1200R-2 2022-05-26 U	sm	- -	9
/2022-07-19T13:32:07/FORS2.2022-05-26T08:17:55.954/	WR4 1200R-2 2022-05-26 L	sg+c	- -	-
/2022-07-19T13:32:07/FORS2.2022-05-28T06:30:20.282/	WR4 1440V-1 2022-05-28 U	sg+c wdeg=4 pd=90	- -	15
/2022-07-19T13:32:07/FORS2.2022-05-28T06:30:20.281/	WR4 1440V-1 2022-05-28 L	sg+c wdeg=4 pd=120	- - evt nochmal	-
/2022-07-19T13:32:07/FORS2.2022-05-28T05:29:42.115/	WR4 1440V-2 2022-05-28 U	sg+c wdeg=4 pd=90	- -	16
/2022-07-19T13:32:07/FORS2.2022-05-28T05:29:42.114/	WR4 1440V-2 2022-05-28 L	sg+c wdeg=4 pd=120	bc see above evt nochmal	-
/2022-07-20T14:59:52/FORS2.2022-05-31T07:35:20.1677/	WR3 1200R-1 2022-05-31 U	sg+c	- -	7
/2022-07-20T14:59:52/FORS2.2022-05-31T07:35:20.166/	WR3 1200R-1 2022-05-31 L	sg+c	- -	Interesting obj. 26/12
/2022-07-20T14:59:52/FORS2.2022-05-31T06:38:52.676/	WR3 1200R-2 2022-05-31 U	sg+c	- -	10
/2022-07-20T14:59:52/FORS2.2022-05-31T06:38:52.677/	WR3 1200R-2 2022-05-31 L	sg+c	- -	-
/2022-07-20T14:59:52/FORS2.2022-07-02T03:13:58.819/	WR3 1200V-1 2022-05-31 U	sg+c	- -	11
/2022-07-20T14:59:52/FORS2.2022-07-02T03:13:58.820/	WR3 1200V-1 2022-05-31 L	sg+c	- -	-
/2022-07-20T14:59:52/FORS2.2022-07-01T04:28:24.722/	WR3 1200V-2 2022-05-31 U	sg+c wdeg=4 pd=90	- -	13
/2022-07-20T14:59:52/FORS2.2022-07-01T04:28:24.721/	WR3 1200V-2 2022-05-31 L	sg+c wdeg=4 pd=80	- -	-
/2022-07-21T14:14:42/FORS2.2022-05-28T07:37:52.416/	WR5 1200R-1 2022-05-28 U	sg+c	- - nicht gut	??
/2022-07-21T14:14:42/FORS2.2022-05-28T07:37:52.417/	WR5 1200R-1 2022-05-28 L	sg+c	- - nicht gut	??
/2022-07-21T14:14:42/FORS2.2022-05-31T05:42:28.017/	WR5 1200R-2 2022-05-31 U	sg+c	- -	??
/2022-07-21T14:14:42/FORS2.2022-05-31T05:42:28.018/	WR5 1200R-2 2022-05-31 L	sg+c	- -	??
/2022-07-21T14:14:42/FORS2.2022-05-29T04:57:16.417/	WR5 1440V-1 2022-05-29 U	sg+c	failed	probably 1
/2022-07-21T14:14:42/FORS2.2022-05-29T04:57:16.418/	WR5 1440V-1 2022-05-29 L	sg+c	failed	-
/2022-07-21T14:14:42/FORS2.2022-05-29T06:19:02.572/	WR5 1440V-2 2022-05-29 U	sm	- -	??
/2022-07-21T14:14:42/FORS2.2022-05-29T06:19:02.573/	WR5 1440V-2 2022-05-29 L	sm	failed	-

Table 26: Paths to Stars. Usually reduced data is saved under reflexdata/reflexendproducts/. If I didn't add something in particular to the notes I used default parameters in the pipeline. sg+c stands for sky global subtraction + cosmic subtraction. U stands for upper CCD in which usually the target star is contained. L stands for lower CCD. sm stands for sky median subtraction

Path	Star	Parameter reduction	Notes	No. of spectrumfile
/2022-08-09T11:06:45/FORS2.2022-05-28T07:37:52.4156/	WR5 1200R-1 2022-05-28 U	default sky local without two cosmetics	low have more extracted spectra	??
/2022-08-09T11:06:45/FORS2.2022-05-31T05:42:28.0177/	WR5 1200R-2 2022-05-31 U	default sky local two cosmetics	- -	??
/2022-08-09T11:06:45/FORS2.2022-05-29T04:57:16.4177/	WR5 1400V-1 2022-05-29 U	default sky local two cosmetics	- -	??
/2022-08-09T11:06:45/FORS2.2022-05-29T06:19:02.5727/	WR5 1400V-2 2022-05-29 U	default sky local two cosmetics	- -	??
/2022-08-24T13:50:09/FORS2.2022-08-27T04:30:44.2547/	WR5 1200R-1 correct 2022-08-24 U	sg+c		3
/2022-08-24T13:50:09/FORS2.2022-08-27T04:30:44.5557/	WR5 1200R-1 correct 2022-08-24 U	sg+c		-
/2022-08-24T13:50:09/FORS2.2022-08-27T03:18:27.6659/	WR5 1200R-2 correct 2022-08-24 U	sg+c		3
/2022-08-24T13:50:09/FORS2.2022-08-27T03:18:27.6659/	WR5 1200R-2 correct 2022-08-24 U	sg+c		-
/2022-08-24T13:50:09/FORS2.2022-08-27T00:57:06.0637/	WR5 1400V-1 correct 2022-08-24 U	sg+c		4
/2022-08-24T13:50:09/FORS2.2022-08-27T00:57:06.0627/	WR5 1400V-1 correct 2022-08-24 U	sg+c		-
/2022-08-24T13:50:09/FORS2.2022-08-27T01:52:38.1267/	WR5 1400V-2 correct 2022-08-24 U	sg+c		4
/2022-08-24T13:50:09/FORS2.2022-08-27T01:52:38.1257/	WR5 1400V-2 correct 2022-08-24 U	sg+c		-

Table 27: Paths to Stars. Usually reduced data is under reflexdata/reflexendproducts/. I will begin with subfolders of these folders for the stellar spectra. If I didn't add something in particular to the notes I used default parameters in the pipeline. sg+c stands for sky global subtraction + cosmic subtraction. U stands for upper CCD in which usually the target star is contained. L stands for lower CCD. sm stands for sky median subtraction

Figure 3: The observation (dark blue) and the SMC WNE 12-12 model (red) with indications which region of the spectrum contributes to the χ^2 value (light blue boxes)



Python programs

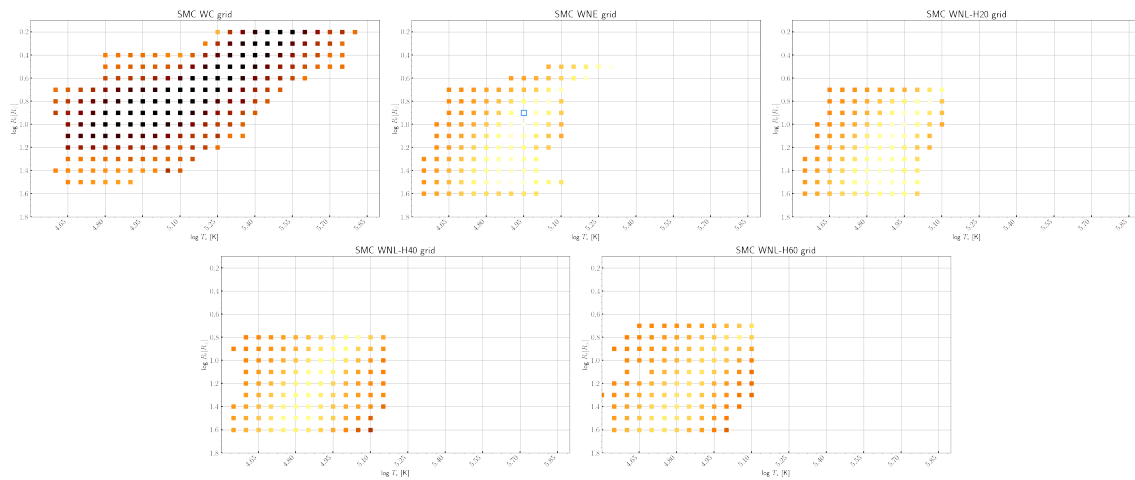
Under `~/jstaehle/Masterthesis/ownpythonscripts/` one can find all additionally written python scripts.

Find grids

`findgrids.ipynb` is a Jupyter notebook containing the χ^2 method of searching for the best model grid spectrum which fits to the observation. One can plot every model grid spectrum on the observation and can see which models fit in which extend to the observation. In the folder there are further notebooks for all my self calculated models and earlier versions of the notebook. It was written by Daniel Pauli and myself.

Since the χ^2 method is not an appropriate approach, I decided to experiment with it to improve it and only make parts of the spectrum contributing to the χ^2 value. To get some help writing the code and getting the Syntax right, I partly worked with Chat-GPT 3.5 which is public available under <https://chat.openai.com/>. It is all commented and indicated which what was done in the file `find_grids_chatgpt`. The best fitting model, compared under all SMC grid models and own calculated models is the grid model SMC 12-12 (see Figure 3): But in this

Figure 4: The χ^2 value evaluated for all SMC model grids. White is the best χ^2 value and black the worst. The best fitting model has a blue square around its position.



model the edges of the lines and some absorption features fit not well to the observation. In Figure 4 it can be seen that also models with up to 40% fit okish. For future work, if you have an observation this program might help you to get in the right direction without testing every model one by one.

fitshandling

`fitshandling.ipynb` is there for you to work with the fits files one get from ESO website. Because of the different directories this can be a little distracting, but it is very useful. With this notebook you can find out where Esoreflex extracted a spectrum, extract the spectrum from the position you want and normalize it using sigma clipping. Additionally, one can get information which is contained in the Fits header. This is very useful for HST images and the Photometry. You can also plot fits image data with ds9 region files, well at least for HST images.

helpfulnotebooks

`beautifulplotting.ipynb` is only a little notebook to plot HRD, spectrum of Nebula faster and in more detail. It lays a focus on design and readability.

`helpful things.ipynb` is a notebook for tiny calculations which are awful to calculate by hand. Sometimes only to check some parameter or to really calculate distances, magnetic field, metallicities, abundances. It is also used to convert wavelength into different units like frequency, energy, temperature

`BinaryWR-OB.ipynb` is cowritten with Daniel Pauli. You can plot a part of your observation and fit one or two gauss functions on a specific line to obtain the radial velocities of each com-

ponent of the binary. Daniel Pauli wrote also a Markov-Chain-Monte-Carlo algorithm in that notebook which was not used for the thesis but it is nice to have a look on it for further projects.

All other programs which are in the folder but are not explained here, are temporary, older or tinier part versions of the ones explained in this appendix.